Efficient treatment of relativistic effects with periodic density functional methods: Energies, gradients, and stress tensors

Yannick J. Franzke [1,2,*] Werner M. Schosser,[3,*] and Fabian Pauly [3,†]

[1]*Fachbereich Chemie, Philipps-Universität Marburg, Hans-Meerwein-Str. 4, 35032 Marburg, Germany*
[2]*Otto Schott Institute of Materials Research, Friedrich Schiller University Jena, Löbdergraben 32, 07743 Jena, Germany*
[3]*Institute of Physics and Center for Advanced Analytics and Predictive Sciences, University of Augsburg,*
Universitätsstr. 1, 86159 Augsburg, Germany

The implementation of an efficient self-consistent field (SCF) method including both scalar-relativistic effects and spin-orbit interaction in density functional theory (DFT) is presented. We make use of Gaussian-type orbitals and all integrals are evaluated in real space. Our implementation supports density functional approximations up to the level of meta-generalized gradient approximations for SCF energies and gradients. The latter can be used to compute the stress tensor and consequently allow us to optimize the cell structure. Considering spin-orbit interaction requires the extension of the standard procedures to a two-component formalism and a noncollinear approach for open-shell systems. Here, we implemented both the canonical and the Scalmani-Frisch noncollinear DFT formalisms, with hybrid and range-separated hybrid functionals being presently restricted to SCF energies. We demonstrate both efficiency and relevance of spin-orbit effects for the electronic structure of discrete systems and systems periodic in one to three dimensions.

I. INTRODUCTION

Modern physics, chemistry, and materials science rely on the theories of quantum mechanics and of special relativity. Particularly for systems that include elements with high nuclear charge, the interplay between both theories is crucial [1–13]. The occurring relativistic effects can be divided into two categories, scalar-relativistic (spin-independent) and spin-dependent relativistic effects. The most prominent scalar-relativistic effects are described by the energy-momentum (or p^4) and the Darwin terms. The dominating spin-dependent relativistic effect is the interaction between the electron's spin and its orbital momentum. For lighter elements, this correction is of negligible or small size and can be treated efficiently with spin-orbit perturbation theory based on the Pauli Hamiltonian [2]. However, for heavy d and p elements, such as platinum, gold, and lead [9,14–16], it is of comparable size as scalar-relativistic effects and thus becomes relevant. Here, more sophisticated spin-orbit perturbation approaches (e.g., Refs. [17–20]) or a variational two-component ansatz treating both relativistic effects on an equal footing are needed.

Spin-dependent relativistic effects are important for solids, surface science, and low-dimensional systems [21–23]. They are exploited in the field of spin-dependent quantum transport for magnetoresistive effects [24–32], for magnetic excitations such as skyrmions [33] caused by the Dzyaloshinskii-Moriya interaction [34,35], and they may lead to spin-polarized surface states of topological insulators [36,37].

Both scalar-relativistic and spin-orbit effects are efficiently modeled by effective core potentials (ECPs) [1,38,39]. Here, the core electrons are replaced with pseudopotentials, which are fitted to high-level relativistic theories. This way, only the one-electron potential operator is directly affected. Therefore, scalar-relativistic effects can be incorporated at essentially no computational burden, as the electron-electron interaction operators are unaffected. However, the description of spin-orbit coupling requires a generalization of the framework. Due to the breakdown of spin symmetry and the complex form of the spin-orbit pseudopotentials or operators, a so-called two-component (2c) formalism employing complex algebra in real space is needed, which leads to an increase of the computational demands [40–50].

Offering relatively low computational costs combined with good accuracy, density functional theory (DFT) is one of the most important computational tools concerning electronic structure theory. For periodic systems, scalar DFT approaches for energies and gradients are widely available in both plane-wave and Gaussian-type orbital (GTO) codes [51–61]. TURBOMOLE [61–65], for instance, includes an efficient and stable program to perform these kinds of calculations for atomic, molecular, and periodic systems, employing GTOs and fast multipole approximations combined with density fitting to ensure time efficiency. However, the functionalities to include spin-orbit interaction for periodic systems are still missing in many program suites, preventing the simulation of promising relativistic systems. Especially open-shell systems require further modifications. That is, a noncollinear formulation of the exchange-correlation potential is needed [40–50]. Moreover, for open-shell systems time-reversal symmetry is artificially broken even in the absence of external

---
*These authors contributed equally to this work.
†fabian.pauly@uni-a.de

fields as a result of the variational optimization in the single-determinant Kohn-Sham (KS) ansatz [66]. In contrast, time-reversal symmetry is well preserved even with a single-determinant KS ansatz for closed-shell systems. The Kramers' theorem can therefore be exploited in these closed-shell cases, considerably simplifying the evaluation of the semilocal exchange-correlation potential.

Recently, a GTO-based noncollinear 2c DFT implementation for periodic systems and self-consistent field (SCF) energies was presented by the group of Erba in the CRYSTAL23 package [50,67–69]. Density functional approximations up to the level of (hybrid) generalized gradient approximations (GGAs) are considered in their work. However, a corresponding implementation of 2c energy gradients has not been presented prior to the original submission of our work (cf. Refs. [70,71,72]). Additionally, meta-generalized gradient approximations (mGGAs) may be superior to GGAs in terms of accuracy [73–86]. Formally, mGGAs require the inclusion of the current density in the kinetic energy density [87–89] for spin-orbit coupling [45] and electromagnetic properties in general [78,90–101,102]. Note that this also applies to the introduction of spin-orbit effects within perturbation theory and linear response methods [93,96]. The impact of the current density in spin-orbit coupling calculations depends on the specific functional and the respective enhancement factors. Here, tests for molecular systems have shown that TASK [77] and the Minnesota functionals such as M06-L [103], M06 [104], or M06-2X [104] are very sensitive to the inclusion of the current density, while TPSS [105] and related functionals are rather insensitive [45,78,91–97,106].

Our work aims to further fill this gap by introducing a 2c formalism to enable simulations of systems with periodic boundary conditions in DFT up to the level of mGGAs including relativistic effects for energies, band structures, energy gradients, and the stress tensor to allow for structure optimizations. For this purpose, existing functionalities for the relativistic treatment of discrete systems with a 2c formalism [43–45] will be introduced into TURBOMOLE's module RIPER [107–113] for periodic electronic structure calculations.

II. THEORY AND IMPLEMENTATION

In this section, we extend the 2c DFT formalism of Armbruster *et al.* [43,44] to periodic systems [107–111] and also consider the noncollinear approach of Scalmani and Frisch [47,48,114] as an alternative to the canonical DFT formalism. Furthermore, the computational demands are assessed and compared to standard one-component (1c) procedures.

A. Two-component SCF formalism

The 2c DFT formalism for periodic systems is based on the quasirelativistic Hamiltonian in the Born-Oppenheimer approximation

$$H^{\vec{L}} = \sum_{i=1}^{n} \left[\boldsymbol{\sigma}_0 h_i^{0,\vec{L}} + \vec{\boldsymbol{\sigma}} \cdot \vec{h}_i^{\mathrm{SO},\vec{L}} \right] + V_{\mathrm{ee}}^{\vec{L}} + V_{\mathrm{NN}}^{\vec{L}} \quad (1)$$

for a unit cell (UC) $\vec{L}$ and n electrons. The terms in the Hamiltonian include an effective spin-orbit (SO) operator

$\vec{\boldsymbol{\sigma}} \cdot \vec{h}_i^{\mathrm{SO},\vec{L}}$, that consists of the standard (2×2) Pauli matrices $\boldsymbol{\sigma}_u$ ($u = x, y, z$) and the vector operator $\vec{h}_i^{\mathrm{SO},\vec{L}}$, which depends on the orbital momentum and parameters fitted to results of, e.g., a relativistic four-component (4c) treatment [1,38,39]. Hence, the operators $\vec{h}_i^{\mathrm{SO},\vec{L}}$ lead to antisymmetric integrals in real space. Further, a spin-independent one-particle Hamiltonian $h_i^{0,\vec{L}}$ that describes the kinetic energy of the electrons and their potential energy in the field of the nuclei is included. $\boldsymbol{\sigma}_0$ is the identity matrix. $V_{\mathrm{ee}}^{\vec{L}}$ and $V_{\mathrm{NN}}^{\vec{L}}$ represent the electron-electron interaction and the repulsion of the nuclei. Additionally, Grimme's DFT dispersion corrections can be handled like the nuclear repulsion operator [115,116]. We stress that the presence of the spin-orbit operator $\vec{\boldsymbol{\sigma}} \cdot \vec{h}_i^{\mathrm{SO},\vec{L}}$ causes the spin not to be a conserved quantity anymore, i.e., the spin is not a "good" quantum number.

The orbital wave functions $\vec{\psi}_i^{\vec{k}}$ thus have to be adjusted. Due to the translational symmetry of solids, they are a linear combination of Bloch functions

$$\phi_\mu^{\vec{k}}(\vec{r}) = \frac{1}{\sqrt{N_{\mathrm{UC}}}} \sum_{\vec{L}} e^{i\vec{k}\cdot\vec{L}} \xi_\mu^{\vec{L}}(\vec{r}) \quad (2)$$

that are expanded in terms of real-valued GTO basis functions

$$\xi_\mu^{\vec{L}}(\vec{r}) = \xi_\mu(\vec{r} - \vec{R}_\mu - \vec{L}), \quad (3)$$

centered at the atomic position $\vec{R}_\mu$ in direct lattice cell $\vec{L}$ over all N_{UC} unit cells. The wave functions are so-called 2c spinors

$$\vec{\psi}_i^{\vec{k}}(\vec{r}) = \begin{pmatrix} \psi_i^{\alpha,\vec{k}}(\vec{r}) \\ \psi_i^{\beta,\vec{k}}(\vec{r}) \end{pmatrix} = \sum_\mu \begin{pmatrix} c_{\mu i}^{\alpha,\vec{k}} \\ c_{\mu i}^{\beta,\vec{k}} \end{pmatrix} \phi_\mu^{\vec{k}}(\vec{r}) \quad (4)$$

with the spin indices α and β, and complex coefficients $c_{\mu i}^{\sigma,\vec{k}}$. The spinors depend on the wave vector $\vec{k}$ within the unit cell in reciprocal space, called the first Brillouin zone (FBZ), and the band index i.

Using this basis-set expansion, the generalized Kohn-Sham (GKS) equations become

$$\begin{pmatrix} \boldsymbol{F}^{\alpha\alpha,\vec{k}} & \boldsymbol{F}^{\alpha\beta,\vec{k}} \\ \boldsymbol{F}^{\beta\alpha,\vec{k}} & \boldsymbol{F}^{\beta\beta,\vec{k}} \end{pmatrix} \begin{pmatrix} \boldsymbol{C}^{\alpha,\vec{k}} \\ \boldsymbol{C}^{\beta,\vec{k}} \end{pmatrix} = \begin{pmatrix} \boldsymbol{S}^{\vec{k}} & \boldsymbol{0} \\ \boldsymbol{0} & \boldsymbol{S}^{\vec{k}} \end{pmatrix} \begin{pmatrix} \boldsymbol{C}^{\alpha,\vec{k}} \\ \boldsymbol{C}^{\beta,\vec{k}} \end{pmatrix} \boldsymbol{\epsilon}^{\vec{k}} \quad (5)$$

with doubled dimension compared to the standard Kohn-Sham formulation. Here, $\boldsymbol{F}$ is the Kohn-Sham-Fock matrix, $\boldsymbol{C}^{\sigma,\vec{k}}$ is the matrix of the spinor coefficients $c_{\mu i}^{\sigma,\vec{k}}$, and $\boldsymbol{\epsilon}^{\vec{k}}$ is the diagonal matrix of the spinor eigenvalues $\epsilon_i^{\sigma,\vec{k}}$. These Roothaan-Hall–type equations can be solved for each $\vec{k}$ point separately in the FBZ. Both the overlap matrix between the GTOs

$$S_{\mu\nu}^{\vec{k}} = \sum_{\vec{L}} e^{i\vec{k}\cdot\vec{L}} S_{\mu\nu}^{\vec{L}} \quad (6)$$

with

$$S_{\mu\nu}^{\vec{L}} = S_{\mu\nu}^{0\vec{L}} = \int \xi_\mu^0(\vec{r}) \xi_\nu^{\vec{L}}(\vec{r}) d^3r \quad (7)$$

and the Kohn-Sham-Fock matrix

$$F_{\mu\nu}^{\vec{k}} = \sum_{\vec{L}} e^{i\vec{k}\cdot\vec{L}} F_{\mu\nu}^{\vec{L}} \qquad (8)$$

are obtained via a Fourier transformation of the real-space matrices. Following Eq. (1), the Kohn-Sham-Fock matrix components are [43]

$$F_{\mu\nu}^{\alpha\alpha,\vec{L}} = T_{\mu\nu}^{\vec{L}} + J_{\mu\nu}^{\vec{L}} + h_{\mu\nu}^{SO,z,\vec{L}} + X_{\mu\nu}^{\alpha\alpha,\vec{L}}, \qquad (9)$$

$$F_{\mu\nu}^{\alpha\beta,\vec{L}} = h_{\mu\nu}^{SO,x,\vec{L}} - ih_{\mu\nu}^{SO,y,\vec{L}} + X_{\mu\nu}^{\alpha\beta,\vec{L}}, \qquad (10)$$

$$F_{\mu\nu}^{\beta\beta,\vec{L}} = T_{\mu\nu}^{\vec{L}} + J_{\mu\nu}^{\vec{L}} - h_{\mu\nu}^{SO,z,\vec{L}} + X_{\mu\nu}^{\beta\beta,\vec{L}}, \qquad (11)$$

consisting of the kinetic energy matrix elements $T_{\mu\nu}^{\vec{L}}$, the Coulomb matrix elements $J_{\mu\nu}^{\vec{L}}$, the exchange-correlation (XC) matrix elements $X_{\mu\nu}^{\sigma\sigma',\vec{L}}$ (with σ and σ' being the spin indices), and the spin-orbit matrix elements $h_{\mu\nu}^{SO,u,\vec{L}}$ ($u = x, y, z$). Thus, the total energy reads as

$$E_{SCF} = E_T + E_J + E_{SO} + E_{XC} + E_{NN} \qquad (12)$$

with the nuclear repulsion term E_{NN}. Note that the scalar ECP contribution $h_{\mu\nu}^{0,\vec{L}}$ is included in the kinetic energy matrix (see below). For open-shell systems without space-inversion symmetry, the Kohn-Sham equations generally need to be solved for $+\vec{k}$ and $-\vec{k}$ explicitly [50].

In this 2c formalism, the general density matrix reads as

$$\boldsymbol{\rho}(\vec{r}, \vec{r}') = \frac{1}{V_{FBZ}} \sum_{i=1}^{n} \int_{FBZ}^{\epsilon_i^{\vec{k}} < \epsilon_F} \vec{\psi}_i^{\vec{k}}(\vec{r})(\vec{\psi}_i^{\vec{k}}(\vec{r}'))^{\dagger} d^3k$$

$$= \begin{pmatrix} \rho^{\alpha\alpha}(\vec{r}, \vec{r}') & \rho^{\alpha\beta}(\vec{r}, \vec{r}') \\ \rho^{\beta\alpha}(\vec{r}, \vec{r}') & \rho^{\beta\beta}(\vec{r}, \vec{r}') \end{pmatrix}. \qquad (13)$$

It involves an integral over the FBZ, V_{FBZ} denotes the volume of the FBZ, and ϵ_F is the Fermi level. The density matrix not only contains the particle contribution

$$\rho_p(\vec{r}, \vec{r}') = Tr[\boldsymbol{\rho}(\vec{r}, \vec{r}')] = \sum_{\vec{L}} Tr[\boldsymbol{\rho}^{\vec{L}}(\vec{r}, \vec{r}')], \qquad (14)$$

but also the spin-vector contribution

$$\vec{\rho}_m(\vec{r}, \vec{r}') = Tr[\vec{\boldsymbol{\sigma}}\boldsymbol{\rho}(\vec{r}, \vec{r}')] = \sum_{\vec{L}} Tr[\vec{\boldsymbol{\sigma}}\boldsymbol{\rho}^{\vec{L}}(\vec{r}, \vec{r}')] \qquad (15)$$

in terms of N_{UC} unit-cell contributions associated with the lattice vectors $\vec{L}$ [cf. Eqs. (2) and (3)]. For easy handling within the program structure, the density matrix $\rho(\vec{r}, \vec{r}')$ is divided into the four spin contributions according to

$$\rho^{\sigma\sigma'}(\vec{r}, \vec{r}') = \sum_{\vec{L}} \rho^{\sigma\sigma',\vec{L}}(\vec{r}, \vec{r}'), \qquad (16)$$

$$\rho^{\sigma\sigma',\vec{L}}(\vec{r}, \vec{r}') = \sum_{\mu\nu} \sum_{\vec{L}'} \xi_{\mu}^{\vec{L}}(\vec{r}) D_{\mu\nu}^{\sigma\sigma',\vec{L}\vec{L}'} \xi_{\nu}^{\vec{L}'}(\vec{r}'). \qquad (17)$$

Thus, the electron density $\rho^{\sigma\sigma'}(\vec{r})$ can be obtained from the atomic-orbital (AO) real-space density matrix

$$D_{\mu\nu}^{\sigma\sigma',\vec{L}\vec{L}'} = \frac{1}{V_{FBZ}} \sum_{i=1}^{n} \int_{FBZ}^{\epsilon_i^{\vec{k}} < \epsilon_F} e^{i\vec{k}\cdot[\vec{L}-\vec{L}']}(c_{\mu i}^{\sigma,\vec{k}} c_{\nu i}^{*\sigma',\vec{k}}) d^3k. \qquad (18)$$

We also define the shorthand notation $D_{\mu\nu}^{\sigma\sigma',\vec{L}} = D_{\mu\nu}^{\sigma\sigma',\vec{L}\vec{0}}$ with

$$D_{\mu\nu}^{\sigma\sigma',\vec{L}} = \frac{1}{V_{FBZ}} \sum_{i=1}^{n} \int_{FBZ}^{\epsilon_i^{\vec{k}} < \epsilon_F} e^{i\vec{k}\cdot\vec{L}}(c_{\mu i}^{\sigma,\vec{k}} c_{\nu i}^{*\sigma',\vec{k}}) d^3k. \qquad (19)$$

Note that the AO density matrix is a complex quantity in the 2c formalism and consists of eight blocks, i.e., four real and four imaginary spin blocks. The particle density $\rho_p(\vec{r}) = \rho_p(\vec{r}, \vec{r})$ relates to the electron number n via

$$\int \rho_p(\vec{r}) \, d^3r = n, \qquad (20)$$

while the spin-vector density or spin-magnetization vector $\vec{\rho}_m(\vec{r}) = \vec{\rho}_m(\vec{r}, \vec{r})$ is related to the expectation value of the system's spin according to

$$\langle \vec{S} \rangle = \frac{1}{2} \int \vec{\rho}_m(\vec{r}) \, d^3r. \qquad (21)$$

In the absence of spin-orbit coupling, this is simply half the number of unpaired or spin-polarized electrons. In terms of AO density matrices, the electron number and the spin expectation value make use of $Re(D_{\mu\nu}^{\alpha\alpha,\vec{L}}) + Re(D_{\mu\nu}^{\beta\beta,\vec{L}})$, and $Re(D_{\mu\nu}^{\alpha\beta,\vec{L}}) + Re(D_{\mu\nu}^{\beta\alpha,\vec{L}})$, $Im(D_{\mu\nu}^{\alpha\beta,\vec{L}}) - Im(D_{\mu\nu}^{\beta\alpha,\vec{L}})$, $Re(D_{\mu\nu}^{\alpha\alpha,\vec{L}}) - Re(D_{\mu\nu}^{\beta\beta,\vec{L}})$, respectively.

Evaluation of the kinetic term

$$T_{\mu\nu}^{\vec{L}} = \int \xi_{\mu}^{\vec{0}}(\vec{r})\left[-\frac{\nabla^2}{2} + V_{sr}^{ECP}(\vec{r})\right]\xi_{\nu}^{\vec{L}}(\vec{r}) \, d^3r, \qquad (22)$$

that also includes scalar-relativistic energy corrections, employing the ECPs V_{sr}^{ECP}, needs no further modification compared to the 1c case, i.e., the elements $T_{\mu\nu}^{\vec{L}}$ form a 1c matrix. Therefore, the respective energy is obtained as

$$E_T = \sum_{\mu\nu} \sum_{\vec{L}} Tr[T_{\mu\nu}^{\vec{L}}\boldsymbol{\sigma}_0 \boldsymbol{D}_{\nu\mu}^{\vec{L}}]$$

$$= \sum_{\mu\nu} \sum_{\vec{L}} T_{\mu\nu}^{\vec{L}}[Re(D_{\nu\mu}^{\alpha\alpha,\vec{L}}) + Re(D_{\nu\mu}^{\beta\beta,\vec{L}})], \qquad (23)$$

where $\boldsymbol{D}_{\nu\mu}^{\vec{L}}$ denotes the (2×2) AO density matrix made up of the four complex spin contributions $D_{\nu\mu}^{\sigma\sigma',\vec{L}}$ [cf. Eq. (19)].

Evaluation of the Coulomb interaction

$$J_{\mu\nu}^{\vec{L}} = \int \xi_{\mu}^{\vec{0}}(\vec{r})\frac{\rho_p(\vec{r}') - \rho_N(\vec{r}')}{|\vec{r} - \vec{r}'|}\xi_{\nu}^{\vec{L}}(\vec{r}) \, d^3r \, d^3r' \qquad (24)$$

utilizes a hierarchical scheme and density fitting [107] with the particle density $\rho_p(\vec{r})$ and the charge distribution $\rho_N(\vec{r})$. The latter is also written as a sum of UC contributions according to

$$\rho_N(\vec{r}) = \sum_{\vec{L}} \rho_N^{\vec{L}}(\vec{r}), \qquad (25)$$

$$\rho_N^{\vec{L}}(\vec{r}) = \sum_{I} Z_I^{eff}\delta(\vec{r} - \vec{R}_I - \vec{L}), \qquad (26)$$

with the effective charges Z_I^{eff} and positions $\vec{R}_I$ of the nuclei I in the reference cell. The 2c implementation of $J_{\mu\nu}^{\vec{L}}$ is straightforward based on the 1c Kohn-Sham scheme, as the Coulomb interaction is independent of the spin and only depends on the particle density. The elements $J_{\mu\nu}^{\vec{L}}$ hence form a 1c matrix.

We refer to Refs. [107,109] for details on the construction of the Coulomb matrix and the corresponding energy. Here, we just state that the Coulomb integrals are split into a crystal near field (CNF) and a crystal far field (CFF), yielding the following two contributions to the Coulomb energy:

$$E_J = E_{J,CNF} + E_{J,CFF}. \tag{27}$$

As the first new terms compared to the 1c formalism, the spin-orbit ECP (SO-ECP) terms $h_{\mu\nu}^{SO,x,\vec{L}}$, $h_{\mu\nu}^{SO,y,\vec{L}}$, and $h_{\mu\nu}^{SO,z,\vec{L}}$ are taken into account. They read as

$$\boldsymbol{h}_{\mu\nu}^{SO,\vec{L}} = \begin{pmatrix} h_{\mu\nu}^{SO,z,\vec{L}} & h_{\mu\nu}^{SO,x,\vec{L}} - ih_{\mu\nu}^{SO,y,\vec{L}} \\ h_{\mu\nu}^{SO,x,\vec{L}} + ih_{\mu\nu}^{SO,y,\vec{L}} & -h_{\mu\nu}^{SO,z,\vec{L}} \end{pmatrix}$$
$$= \int \xi_\mu^{\vec{0}}(\vec{r}) \boldsymbol{V}_{SO}^{ECP}(\vec{r}) \xi_\nu^{\vec{L}}(\vec{r}) \, d^3r \tag{28}$$

with the effective spin-orbit potential $\boldsymbol{V}_{SO}^{ECP}(\vec{r})$. The associated spin-orbit energy is obtained as

$$E_{SO} = \sum_{\mu\nu} \sum_{\vec{L}} \text{Tr}\big[\boldsymbol{h}_{\mu\nu}^{SO,\vec{L}} \boldsymbol{D}_{\nu\mu}^{\vec{L}}\big]. \tag{29}$$

Here, the antisymmetric linear combinations of the AO density matrices are needed, i.e., $\text{Im}(D_{\nu\mu}^{\alpha\beta,\vec{L}}) + \text{Im}(D_{\nu\mu}^{\beta\alpha,\vec{L}})$, $\text{Re}(D_{\nu\mu}^{\alpha\beta,\vec{L}}) - \text{Re}(D_{\nu\mu}^{\beta\alpha,\vec{L}})$, and $\text{Im}(D_{\nu\mu}^{\alpha\alpha,\vec{L}}) - \text{Im}(D_{\nu\mu}^{\beta\beta,\vec{L}})$ for the spin-orbit x, y, and z components, respectively. These density matrices also give rise to a spin-current density contribution [45]. In contrast, E_{SO} does not depend explicitly on the particle current density.

The final term, that has to be considered, involves the exchange-correlation matrices $\boldsymbol{X}^{\sigma\sigma'}$. We will first discuss the semilocal or "pure" (i.e., nonhybrid) contributions and then describe the generalization to include Fock exchange. The semilocal XC matrices not only depend on the particle-number density ρ_p but also on the spin-vector density or spin-magnetization vector $\vec{\rho}_m$. In the noncollinear Kramers-unrestricted (KU) formalism, the XC potential operator of the local spin density approximation is given by

$$\boldsymbol{V}^{XC}[\rho_p(\vec{r}), \vec{\rho}_m(\vec{r})] = \frac{\delta E_{XC}}{\delta \rho_p(\vec{r})} \boldsymbol{\sigma}_0 + \sum_{u=\{x,y,z\}} \frac{\delta E_{XC}}{\delta \rho_{m,u}(\vec{r})} \boldsymbol{\sigma}_u$$
$$= \frac{\delta E_{XC}}{\delta \rho_p(\vec{r})} \boldsymbol{\sigma}_0 + \frac{\delta E_{XC}}{\delta |\vec{\rho}_m(\vec{r})|} \frac{\vec{\rho}_m(\vec{r}) \cdot \vec{\boldsymbol{\sigma}}}{|\vec{\rho}_m(\vec{r})|}. \tag{30}$$

It is based on the exchange-correlation energy as a functional of the particle density and the norm of the spin-vector density

$$E_{XC} = E_{XC}[\rho_p(\vec{r}), |\vec{\rho}_m(\vec{r})|] = E_{XC}[\rho_{\uparrow,\downarrow}(\vec{r})], \tag{31}$$

$$\rho_{\uparrow,\downarrow}(\vec{r}) = \tfrac{1}{2}[\rho_p(\vec{r}) \pm |\vec{\rho}_m(\vec{r})|]. \tag{32}$$

More generally, the semilocal XC energy for a given density functional approximation f^{XC} reads as

$$E_{XC} = \int_{UC} f^{XC}[\rho_{\uparrow,\downarrow}(\vec{r}), \gamma_{\uparrow\uparrow,\uparrow\downarrow,\downarrow\downarrow}(\vec{r}), \tau_{\uparrow,\downarrow}(\vec{r})] \, d^3r, \tag{33}$$

using the auxiliary variable $\gamma_{\sigma\sigma'} = \frac{1}{4}(\vec{\nabla}\rho_\sigma) \cdot (\vec{\nabla}\rho_{\sigma'})$ with $\sigma, \sigma' \in \{\uparrow, \downarrow\}$ and the kinetic energy density τ for mGGAs. The kinetic energy density may be defined analogously to the

electron density as

$$\boldsymbol{\tau}(\vec{r}, \vec{r}\,') = \frac{1}{V_{FBZ}} \sum_{i=1}^n \int_{FBZ}^{\epsilon_i^{\vec{k}} < \epsilon_F} \big(\vec{\nabla}\vec{\psi}_i^{\vec{k}}(\vec{r})\big)\big(\vec{\nabla}\vec{\psi}_i^{\vec{k}}(\vec{r}\,')\big)^\dagger d^3k. \tag{34}$$

The particle kinetic energy density and the spin contributions then follow as

$$\tau_p(\vec{r}) = \text{Tr}[\boldsymbol{\tau}(\vec{r})] = \text{Tr}[\boldsymbol{\tau}(\vec{r}, \vec{r})], \tag{35}$$

$$\vec{\tau}_m(\vec{r}) = \text{Tr}[\vec{\boldsymbol{\sigma}}\boldsymbol{\tau}(\vec{r})] = \text{Tr}[\vec{\boldsymbol{\sigma}}\boldsymbol{\tau}(\vec{r}, \vec{r})], \tag{36}$$

which allow to construct $\tau_{\uparrow,\downarrow}(\vec{r})$ analogously to Eq. (32). We note that the current density correction for $\boldsymbol{\tau}(\vec{r}, \vec{r}\,')$ is presently neglected in RIPER, while we have implemented it for molecular systems [45]. Therefore, only the real and symmetric parts of the spin magnetization in direct space are used for the semilocal XC contribution in RIPER, i.e.,

$$\rho_m^x(\vec{r}) = \rho^{\alpha\beta}(\vec{r}) + \rho^{\beta\alpha}(\vec{r}), \tag{37}$$

$$\rho_m^y(\vec{r}) = i(\rho^{\alpha\beta}(\vec{r}) - \rho^{\beta\alpha}(\vec{r})), \tag{38}$$

$$\rho_m^z(\vec{r}) = \rho^{\alpha\alpha}(\vec{r}) - \rho^{\beta\beta}(\vec{r}). \tag{39}$$

In terms of AO density matrices, we need the symmetric linear combinations $\text{Re}(D_{\nu\mu}^{\alpha\beta,\vec{L}}) + \text{Re}(D_{\nu\mu}^{\beta\alpha,\vec{L}})$, $\text{Im}(D_{\nu\mu}^{\alpha\beta,\vec{L}}) - \text{Im}(D_{\nu\mu}^{\beta\alpha,\vec{L}})$, and $\text{Re}(D_{\nu\mu}^{\alpha\alpha,\vec{L}}) - \text{Re}(D_{\nu\mu}^{\beta\beta,\vec{L}})$ for the noncollinear x, y, and z components.

For an implementation with real AO basis functions, it is advantageous to directly calculate the semilocal exchange-correlation potential in a matrix representation as

$$X_{\mu\nu}^{\vec{L}} = \int \xi_\mu^{\vec{0}}(\vec{r}) V^{XC}(\vec{r}) \xi_\nu^{\vec{L}}(\vec{r}) d^3r \tag{40}$$

by differentiation of the exchange-correlation energy with respect to the corresponding AO density matrices [117]. Thus, the quantities for the 2c formalism follow as

$$X_{\mu\nu}^{0,\vec{L}} = \int \frac{1}{2}\bigg[\frac{\partial f^{XC}}{\partial \rho_\uparrow} + \frac{\partial f^{XC}}{\partial \rho_\downarrow}\bigg] \xi_\mu^{\vec{0}}(\vec{r}) \, \xi_\nu^{\vec{L}}(\vec{r}) \, d^3r$$
$$- \int \frac{1}{2}\bigg[2\frac{\partial f^{XC}}{\partial \gamma_{\uparrow\uparrow}}\vec{\nabla}\rho_\uparrow + 2\frac{\partial f^{XC}}{\partial \gamma_{\downarrow\downarrow}}\vec{\nabla}\rho_\downarrow$$
$$+ \frac{\partial f^{XC}}{\partial \gamma_{\uparrow\downarrow}}(\vec{\nabla}\rho_\uparrow + \vec{\nabla}\rho_\downarrow)\bigg]$$
$$\cdot \big[\{\vec{\nabla}\xi_\mu^{\vec{0}}(\vec{r})\}\xi_\nu^{\vec{L}}(\vec{r}) + \xi_\mu^{\vec{0}}(\vec{r})\{\vec{\nabla}\xi_\nu^{\vec{L}}(\vec{r})\}\big]d^3r$$
$$+ \int \frac{1}{2}\bigg[\frac{\partial f^{XC}}{\partial \tau_\uparrow} + \frac{\partial f^{XC}}{\partial \tau_\downarrow}\bigg]\big[\vec{\nabla}\xi_\mu^{\vec{0}}(\vec{r})\big] \cdot \big[\vec{\nabla}\xi_\nu^{\vec{L}}(\vec{r})\big]d^3r \tag{41}$$

for the scalar contribution, which is multiplied with $\boldsymbol{\sigma}_0$, and

$$X_{\mu\nu}^{u,\vec{L}} = \frac{\rho_m^u}{|\vec{\rho}_m|}\bigg\{ \int \frac{1}{2}\bigg[\frac{\partial f^{XC}}{\partial \rho_\uparrow} - \frac{\partial f^{XC}}{\partial \rho_\downarrow}\bigg]\xi_\mu^{\vec{0}}(\vec{r}) \, \xi_\nu^{\vec{L}}(\vec{r}) \, d^3r$$
$$- \int \frac{1}{2}\bigg[2\frac{\partial f^{XC}}{\partial \gamma_{\uparrow\uparrow}}\vec{\nabla}\rho_\uparrow - 2\frac{\partial f^{XC}}{\partial \gamma_{\downarrow\downarrow}}\vec{\nabla}\rho_\downarrow$$

$$- \frac{\partial f^{XC}}{\partial \gamma_{\uparrow\downarrow}} (\vec{\nabla}\rho_\uparrow - \vec{\nabla}\rho_\downarrow) \Big]$$
$$\cdot \Big[\{\vec{\nabla}\xi_\mu^{\bar{0}}(\vec{r})\}\xi_\nu^{\bar{L}}(\vec{r}) + \xi_\mu^{\bar{0}}(\vec{r})\{\vec{\nabla}\xi_\nu^{\bar{L}}(\vec{r})\} \Big] d^3r$$
$$+ \int \frac{1}{2}\Big[\frac{\partial f^{XC}}{\partial \tau_\uparrow} - \frac{\partial f^{XC}}{\partial \tau_\downarrow} \Big][\vec{\nabla}\xi_\mu^{\bar{0}}(\vec{r})]\cdot[\vec{\nabla}\xi_\nu^{\bar{L}}(\vec{r})]d^3r \Big\}$$
$$(42)$$

for the spin contributions with $u \in \{x,y,z\}$. The four spin blocks for the Kohn-Sham-Fock equations [cf. Eqs. (9)–(11)] can be evaluated from Eqs. (41) and (42) according to

$$X_{\mu\nu}^{\alpha\alpha,\bar{L}} = \tfrac{1}{2}\big(X_{\mu\nu}^{0,\bar{L}} + X_{\mu\nu}^{z,\bar{L}}\big), \tag{43}$$

$$X_{\mu\nu}^{\beta\beta,\bar{L}} = \tfrac{1}{2}\big(X_{\mu\nu}^{0,\bar{L}} - X_{\mu\nu}^{z,\bar{L}}\big), \tag{44}$$

$$X_{\mu\nu}^{\alpha\beta,\bar{L}} = \tfrac{1}{2}\big(X_{\mu\nu}^{x,\bar{L}} - iX_{\mu\nu}^{y,\bar{L}}\big), \tag{45}$$

$$X_{\mu\nu}^{\beta\alpha,\bar{L}} = \tfrac{1}{2}\big(X_{\mu\nu}^{x,\bar{L}} - iX_{\mu\nu}^{y,\bar{L}}\big)^*. \tag{46}$$

We note that this form is a well-established approximation in relativistic quantum mechanics [49]. The evaluation of the exchange-correlation matrix blocks uses numerical integration on a grid and the hierarchical scheme presented in Ref. [108]. Details on the underlying molecular 2c implementation can be found in Refs. [43–45].

Equations (41) and (42) correspond to the canonical non-collinear formalism [40,42]. An alternative approach with a local magnetic torque was presented by Scalmani and Frisch (SF) [47] for molecules and later extended to periodic systems in Ref. [48]. This approach is numerically slightly more stable than the canonical ansatz [49]. The following generalizations are used for the extension of the unrestricted Kohn-Sham (UKS) framework to the GKS picture:

$$\gamma_{\uparrow\uparrow,\downarrow\downarrow}^{SF} = \frac{1}{4}[\vec{\nabla}\rho_p \cdot \vec{\nabla}\rho_p + \vec{\nabla}\vec{\rho}_m \odot \vec{\nabla}\vec{\rho}_m] \pm \frac{f_\nabla}{2}\Gamma, \quad (47)$$

$$\Gamma = \sqrt{(\vec{\nabla}\rho_p \cdot \vec{\nabla}\vec{\rho}_m)\circ(\vec{\nabla}\rho_p \cdot \vec{\nabla}\vec{\rho}_m)}, \tag{48}$$

$$\gamma_{\uparrow\downarrow}^{SF} = \frac{1}{4}[\vec{\nabla}\rho_p \cdot \vec{\nabla}\rho_p - \vec{\nabla}\vec{\rho}_m \odot \vec{\nabla}\vec{\rho}_m], \tag{49}$$

$$f_\nabla = \text{sgn}([\vec{\nabla}\rho_p \cdot \vec{\nabla}\vec{\rho}_m]\circ \vec{\rho}_m), \tag{50}$$

$$\tau_{\uparrow,\downarrow}^{SF} = \frac{1}{2}\tau_p \pm \frac{f_\tau}{2}|\vec{\tau}_m|, \tag{51}$$

$$f_\tau = \text{sgn}(\vec{\tau}_m \circ \vec{\rho}_m). \tag{52}$$

Here, sgn is the signum function and $\circ$ indicates a scalar product of spin components, while the center dot ($\cdot$) refers to the scalar product in real space. Simultaneous scalar products are denoted with $\odot$ according to

$$\vec{\nabla}\vec{\rho}_m \odot \vec{\nabla}\vec{\rho}_m = \sum_{u\in\{x,y,z\}} (\vec{\nabla}\rho_m^u)\cdot(\vec{\nabla}\rho_m^u). \tag{53}$$

The densities $\rho_\uparrow^{SF}$ and $\rho_\downarrow^{SF}$ are the same as for the canonical ansatz [47], i.e., $\rho_\uparrow$ and $\rho_\downarrow$ of Eq. (32). The semilocal XC potential is again obtained via derivatives with respect to the AO density matrices [114], and this results in the scalar XC

contribution

$$X_{\mu\nu}^{SF,0,\bar{L}} = \int \frac{1}{2}\Big[\frac{\partial f^{XC}}{\partial \rho_\uparrow^{SF}} + \frac{\partial f^{XC}}{\partial \rho_\downarrow^{SF}} \Big]\xi_\mu^{\bar{0}}(\vec{r})\,\xi_\nu^{\bar{L}}(\vec{r})\,d^3r$$
$$- \int \frac{1}{2}\Big[\frac{\partial f^{XC}}{\partial \gamma_{\uparrow\uparrow}^{SF}} + \frac{\partial f^{XC}}{\partial \gamma_{\downarrow\downarrow}^{SF}} + \frac{\partial f^{XC}}{\partial \gamma_{\uparrow\downarrow}^{SF}} \Big]\vec{\nabla}\rho_p$$
$$\cdot \Big[\{\vec{\nabla}\xi_\mu^{\bar{0}}(\vec{r})\}\xi_\nu^{\bar{L}}(\vec{r}) + \xi_\mu^{\bar{0}}(\vec{r})\{\vec{\nabla}\xi_\nu^{\bar{L}}(\vec{r})\} \Big]d^3r$$
$$- \int \Big[\frac{\partial f^{XC}}{\partial \gamma_{\uparrow\uparrow}^{SF}} - \frac{\partial f^{XC}}{\partial \gamma_{\downarrow\downarrow}^{SF}} \Big]\frac{f_\nabla}{2}\frac{(\vec{\nabla}\rho_p \cdot \vec{\nabla}\vec{\rho}_m)\circ\vec{\nabla}\vec{\rho}_m}{\Gamma}$$
$$\cdot \Big[\{\vec{\nabla}\xi_\mu^{\bar{0}}(\vec{r})\}\xi_\nu^{\bar{L}}(\vec{r}) + \xi_\mu^{\bar{0}}(\vec{r})\{\vec{\nabla}\xi_\nu^{\bar{L}}(\vec{r})\} \Big]d^3r$$
$$+ \int \frac{1}{2}\Big[\frac{\partial f^{XC}}{\partial \tau_\uparrow^{SF}} + \frac{\partial f^{XC}}{\partial \tau_\downarrow^{SF}} \Big][\vec{\nabla}\xi_\mu^{\bar{0}}(\vec{r})]\cdot[\vec{\nabla}\xi_\nu^{\bar{L}}(\vec{r})]d^3r$$
$$(54)$$

and the three spin-orbit contributions

$$X_{\mu\nu}^{SF,u,\bar{L}} = \frac{\rho_m^u}{|\vec{\rho}_m|}\int \frac{1}{2}\Big[\frac{\partial f^{XC}}{\partial \rho_\uparrow^{SF}} - \frac{\partial f^{XC}}{\partial \rho_\downarrow^{SF}} \Big]\xi_\mu^{\bar{0}}(\vec{r})\,\xi_\nu^{\bar{L}}(\vec{r})\,d^3r$$
$$- \int \frac{1}{2}\Big[\frac{\partial f^{XC}}{\partial \gamma_{\uparrow\uparrow}^{SF}} + \frac{\partial f^{XC}}{\partial \gamma_{\downarrow\downarrow}^{SF}} - \frac{\partial f^{XC}}{\partial \gamma_{\uparrow\downarrow}^{SF}} \Big]\vec{\nabla}\rho_m^u$$
$$\cdot \Big[\{\vec{\nabla}\xi_\mu^{\bar{0}}(\vec{r})\}\xi_\nu^{\bar{L}}(\vec{r}) + \xi_\mu^{\bar{0}}(\vec{r})\{\vec{\nabla}\xi_\nu^{\bar{L}}(\vec{r})\} \Big]d^3r$$
$$- \int \Big[\frac{\partial f^{XC}}{\partial \gamma_{\uparrow\uparrow}^{SF}} - \frac{\partial f^{XC}}{\partial \gamma_{\downarrow\downarrow}^{SF}} \Big]\frac{f_\nabla}{2}\frac{(\vec{\nabla}\rho_p \cdot \vec{\nabla}\rho_m^u)\vec{\nabla}\rho_p}{\Gamma}$$
$$\cdot \Big[\{\vec{\nabla}\xi_\mu^{\bar{0}}(\vec{r})\}\xi_\nu^{\bar{L}}(\vec{r}) + \xi_\mu^{\bar{0}}(\vec{r})\{\vec{\nabla}\xi_\nu^{\bar{L}}(\vec{r})\} \Big]d^3r$$
$$+ \int \Big[\frac{\partial f^{XC}}{\partial \tau_\uparrow^{SF}} - \frac{\partial f^{XC}}{\partial \tau_\downarrow^{SF}} \Big]\frac{f_\tau}{2}\frac{\tau_m^u}{|\vec{\tau}_m|}[\vec{\nabla}\xi_\mu^{\bar{0}}(\vec{r})]\cdot[\vec{\nabla}\xi_\nu^{\bar{L}}(\vec{r})]d^3r.$$
$$(55)$$

The denominator including Γ is detrimental for some applications as noted in Ref. [114]. That is, another transformation is used for regions with a small magnetization length, i.e., spatial regions with $|\vec{\rho}_m(\vec{r})| < 10^{-12}$ in atomic units. The expressions for this modified Scalmani-Frisch (mSF) formalism read as

$$\rho_{\uparrow\uparrow,\downarrow\downarrow}^{mSF} = \frac{1}{2}[\rho_p \pm \rho_s], \tag{56}$$

$$\rho_s = \frac{1}{3}\big[\rho_m^x + \rho_m^y + \rho_m^z\big], \tag{57}$$

$$\gamma_{\uparrow\uparrow,\downarrow\downarrow}^{mSF} = \frac{1}{4}[\vec{\nabla}\rho_p \cdot \vec{\nabla}\rho_p + \vec{\nabla}\vec{\rho}_m \odot \vec{\nabla}\vec{\rho}_m] \pm \frac{f_\nabla}{2}\Gamma_s, \quad (58)$$

$$\Gamma_s = \vec{\nabla}\rho_p \cdot \vec{\nabla}\rho_s, \tag{59}$$

$$\gamma_{\uparrow\downarrow}^{mSF} = \frac{1}{4}[\vec{\nabla}\rho_p \cdot \vec{\nabla}\rho_p - \vec{\nabla}\vec{\rho}_m \odot \vec{\nabla}\vec{\rho}_m], \tag{60}$$

$$\tau_{\uparrow,\downarrow}^{mSF} = \frac{1}{2}\tau_p \pm \frac{f_\tau}{2}\tau_s, \tag{61}$$

$$\tau_s = \frac{1}{3}\big[\tau_m^x + \tau_m^y + \tau_m^z\big]. \tag{62}$$

This leads to the semilocal XC potential matrices

$$
\begin{aligned}
X_{\mu\nu}^{\mathrm{mSF},0,\vec{L}} = & \int \frac{1}{2}\left[\frac{\partial f^{\mathrm{XC}}}{\partial \rho_\uparrow^{\mathrm{mSF}}} + \frac{\partial f^{\mathrm{XC}}}{\partial \rho_\downarrow^{\mathrm{mSF}}}\right]\xi_\mu^{\vec{0}}(\vec{r})\,\xi_\nu^{\vec{L}}(\vec{r})\,d^3r \\
& - \int \frac{1}{2}\left[\frac{\partial f^{\mathrm{XC}}}{\partial \gamma_{\uparrow\uparrow}^{\mathrm{mSF}}} + \frac{\partial f^{\mathrm{XC}}}{\partial \gamma_{\downarrow\downarrow}^{\mathrm{mSF}}} + \frac{\partial f^{\mathrm{XC}}}{\partial \gamma_{\uparrow\downarrow}^{\mathrm{mSF}}}\right]\vec{\nabla}\rho_{\mathrm{p}} \\
& \cdot \left[\left\{\vec{\nabla}\xi_\mu^{\vec{0}}(\vec{r})\right\}\xi_\nu^{\vec{L}}(\vec{r}) + \xi_\mu^{\vec{0}}(\vec{r})\left\{\vec{\nabla}\xi_\nu^{\vec{L}}(\vec{r})\right\}\right]d^3r \\
& - \int \left[\frac{\partial f^{\mathrm{XC}}}{\partial \gamma_{\uparrow\uparrow}^{\mathrm{mSF}}} - \frac{\partial f^{\mathrm{XC}}}{\partial \gamma_{\downarrow\downarrow}^{\mathrm{mSF}}}\right]\frac{f_\nabla}{2}\vec{\nabla}\rho_{\mathrm{s}} \\
& \cdot \left[\left\{\vec{\nabla}\xi_\mu^{\vec{0}}(\vec{r})\right\}\xi_\nu^{\vec{L}}(\vec{r}) + \xi_\mu^{\vec{0}}(\vec{r})\left\{\vec{\nabla}\xi_\nu^{\vec{L}}(\vec{r})\right\}\right]d^3r \\
& + \int \frac{1}{2}\left[\frac{\partial f^{\mathrm{XC}}}{\partial \tau_\uparrow^{\mathrm{mSF}}} + \frac{\partial f^{\mathrm{XC}}}{\partial \tau_\downarrow^{\mathrm{mSF}}}\right]\left[\vec{\nabla}\xi_\mu^{\vec{0}}(\vec{r})\right]\cdot\left[\vec{\nabla}\xi_\nu^{\vec{L}}(\vec{r})\right]d^3r
\end{aligned}
\tag{63}
$$

and

$$
\begin{aligned}
X_{\mu\nu}^{\mathrm{mSF},u,\vec{L}} = & \int \frac{1}{6}\left[\frac{\partial f^{\mathrm{XC}}}{\partial \rho_\uparrow^{\mathrm{mSF}}} - \frac{\partial f^{\mathrm{XC}}}{\partial \rho_\downarrow^{\mathrm{mSF}}}\right]\xi_\mu^{\vec{0}}(\vec{r})\,\xi_\nu^{\vec{L}}(\vec{r})\,d^3r \\
& - \int \frac{1}{2}\left[\frac{\partial f^{\mathrm{XC}}}{\partial \gamma_{\uparrow\uparrow}^{\mathrm{mSF}}} + \frac{\partial f^{\mathrm{XC}}}{\partial \gamma_{\downarrow\downarrow}^{\mathrm{mSF}}} - \frac{\partial f^{\mathrm{XC}}}{\partial \gamma_{\uparrow\downarrow}^{\mathrm{mSF}}}\right]\vec{\nabla}\rho_{\mathrm{m}}^u \\
& \cdot \left[\left\{\vec{\nabla}\xi_\mu^{\vec{0}}(\vec{r})\right\}\xi_\nu^{\vec{L}}(\vec{r}) + \xi_\mu^{\vec{0}}(\vec{r})\left\{\vec{\nabla}\xi_\nu^{\vec{L}}(\vec{r})\right\}\right]d^3r \\
& - \int \left[\frac{\partial f^{\mathrm{XC}}}{\partial \gamma_{\uparrow\uparrow}^{\mathrm{mSF}}} - \frac{\partial f^{\mathrm{XC}}}{\partial \gamma_{\downarrow\downarrow}^{\mathrm{mSF}}}\right]\frac{f_\nabla}{6}\vec{\nabla}\rho_{\mathrm{p}} \\
& \cdot \left[\left\{\vec{\nabla}\xi_\mu^{\vec{0}}(\vec{r})\right\}\xi_\nu^{\vec{L}}(\vec{r}) + \xi_\mu^{\vec{0}}(\vec{r})\left\{\vec{\nabla}\xi_\nu^{\vec{L}}(\vec{r})\right\}\right]d^3r \\
& + \int \left[\frac{\partial f^{\mathrm{XC}}}{\partial \tau_\uparrow^{\mathrm{mSF}}} - \frac{\partial f^{\mathrm{XC}}}{\partial \tau_\downarrow^{\mathrm{mSF}}}\right]\frac{f_\tau}{6}\left[\vec{\nabla}\xi_\mu^{\vec{0}}(\vec{r})\right]\cdot\left[\vec{\nabla}\xi_\nu^{\vec{L}}(\vec{r})\right]d^3r.
\end{aligned}
\tag{64}
$$

The noncollinear formalism is needed for open-shell systems. For closed-shell systems, the real and symmetric parts of the spin-vector density matrix vanish due to Kramers' theorem, i.e., $\mathrm{Re}(D_{\nu\mu}^{\alpha\beta,\vec{L}}) + \mathrm{Re}(D_{\nu\mu}^{\beta\alpha,\vec{L}})$, $\mathrm{Im}(D_{\nu\mu}^{\alpha\beta,\vec{L}}) - \mathrm{Im}(D_{\nu\mu}^{\beta\alpha,\vec{L}})$, and $\mathrm{Re}(D_{\nu\mu}^{\alpha\alpha,\vec{L}}) - \mathrm{Re}(D_{\nu\mu}^{\beta\beta,\vec{L}})$ are zero. Further, time-reversal symmetry holds. Therefore, the general or unrestricted 2c formalism can be reduced to a Kramers-restricted (KR) framework and the semilocal XC potential can be evaluated as done in the 1c formalism.

Hybrid density functionals [73,81,118] include a portion of nonlocal Fock exchange. Thus, the exchange-correlation matrix becomes

$$
\boldsymbol{X}^{\sigma\sigma'} = \boldsymbol{X}_{\mathrm{C}}^{\sigma\sigma'} + (1-a)\boldsymbol{X}_{\mathrm{X}}^{\sigma\sigma'} + a\boldsymbol{K}^{\sigma\sigma'}
\tag{65}
$$

with $\boldsymbol{X}_{\mathrm{C}}^{\sigma\sigma'}$ and $\boldsymbol{X}_{\mathrm{X}}^{\sigma\sigma'}$ denoting the semilocal DFT correlation and exchange contributions discussed so far, and a is the mixing parameter. The Fock exchange matrix $\boldsymbol{K}^{\sigma\sigma'}$

reads as

$$
\begin{aligned}
K_{\mu\nu}^{\sigma\sigma',\vec{L}\vec{L}'} = & \sum_{\lambda\kappa}\sum_{\vec{M}\vec{N}} D_{\lambda\kappa}^{\sigma\sigma',\vec{M}\vec{N}} \iint \left[\xi_\mu^{\vec{L}}(\vec{r})\,\xi_\kappa^{\vec{N}}(\vec{r}\,')\right. \\
& \left.\times \frac{1}{|\vec{r}-\vec{r}\,'|}\,\xi_\lambda^{\vec{M}}(\vec{r})\,\xi_\nu^{\vec{L}'}(\vec{r}\,')\right]d^3r\,d^3r'
\end{aligned}
\tag{66}
$$

with $\vec{L}$, $\vec{L}'$, $\vec{M}$, $\vec{N}$ referring to lattice vectors. For range-separated hybrid functionals, the two-electron interaction operator is replaced with an effective operator [119–122]. The respective 2c complex form reads as [48]

$$
\boldsymbol{K}^{\vec{L}\vec{L}'} = \begin{pmatrix} \boldsymbol{K}^{\alpha\alpha} & \boldsymbol{K}^{\alpha\beta} \\ \boldsymbol{K}^{\beta\alpha} & \boldsymbol{K}^{\beta\beta} \end{pmatrix}^{\vec{L}\vec{L}'}
\tag{67}
$$

using all blocks of the 2c complex AO density matrix, i.e., the particle and spin density contributions $\mathrm{Re}(D_{\nu\mu}^{\alpha\alpha,\vec{M}\vec{N}}) + \mathrm{Re}(D_{\nu\mu}^{\beta\beta,\vec{M}\vec{N}})$, $\mathrm{Re}(D_{\nu\mu}^{\alpha\beta,\vec{M}\vec{N}}) + \mathrm{Re}(D_{\nu\mu}^{\beta\alpha,\vec{M}\vec{N}})$, $\mathrm{Im}(D_{\nu\mu}^{\alpha\beta,\vec{M}\vec{N}}) - \mathrm{Im}(D_{\nu\mu}^{\beta\alpha,\vec{M}\vec{N}})$, $\mathrm{Re}(D_{\nu\mu}^{\alpha\alpha,\vec{M}\vec{N}}) - \mathrm{Re}(D_{\nu\mu}^{\beta\beta,\vec{M}\vec{N}})$, as well as $\mathrm{Im}(D_{\nu\mu}^{\alpha\alpha,\vec{M}\vec{N}}) + \mathrm{Im}(D_{\nu\mu}^{\beta\beta,\vec{M}\vec{N}})$, $\mathrm{Im}(D_{\nu\mu}^{\alpha\beta,\vec{M}\vec{N}}) + \mathrm{Im}(D_{\nu\mu}^{\beta\alpha,\vec{M}\vec{N}})$, $\mathrm{Re}(D_{\nu\mu}^{\alpha\beta,\vec{M}\vec{N}}) - \mathrm{Re}(D_{\nu\mu}^{\beta\alpha,\vec{M}\vec{N}})$, and $\mathrm{Im}(D_{\nu\mu}^{\alpha\alpha,\vec{M}\vec{N}}) - \mathrm{Im}(D_{\nu\mu}^{\beta\beta,\vec{M}\vec{N}})$. The latter four linear combinations are related to the particle current density and the three spin-current densities [50]. Thus, Fock exchange naturally includes the current density in the formalism and also features a local magnetic torque as discussed in Ref. [50]. However, the semilocal DFT exchange and correlation parts still do not explicitly depend on the current density.

Based on the eight linear combinations above, the 2c Fock exchange can be evaluated straightforwardly as discussed in Ref. [48]. In this spirit, we extended the implementation of Ref. [112], making use of a minimum image convention or the truncated Coulomb interaction to the 2c formalism.

For closed-shell Kramers-restricted systems, the spin density and particle current density contributions vanish also for the Fock exchange. However, the spin-current density contributions, i.e., the three linear combinations $\mathrm{Im}(D_{\nu\mu}^{\alpha\beta,\vec{M}\vec{N}}) + \mathrm{Im}(D_{\nu\mu}^{\beta\alpha,\vec{M}\vec{N}})$, $\mathrm{Re}(D_{\nu\mu}^{\alpha\beta,\vec{M}\vec{N}}) - \mathrm{Re}(D_{\nu\mu}^{\beta\alpha,\vec{M}\vec{N}})$, and $\mathrm{Im}(D_{\nu\mu}^{\alpha\alpha,\vec{M}\vec{N}}) - \mathrm{Im}(D_{\nu\mu}^{\beta\beta,\vec{M}\vec{N}})$, are not necessarily zero. Thus, the 2c formulation of the Fock exchange still requires changes of the underlying 1c code for Kramers-restricted calculations.

B. Two-component energy gradients

Energy gradients are required to optimize coordinates of atoms in the unit cell and to optimize the corresponding lattice vectors based on the stress tensor [110,123–127]. Here, we neglect Fock exchange and only consider semilocal or "pure" density functional approximations. The derivative of the SCF energy with respect to a nuclear displacement reads as

$$
E_{\mathrm{SCF}}^{I,\lambda} = E_{\mathrm{T}}^{I,\lambda} + E_{\mathrm{J}}^{I,\lambda} + E_{\mathrm{SO}}^{I,\lambda} + E_{\mathrm{XC}}^{I,\lambda} + E_{\mathrm{NN}}^{I,\lambda},
\tag{68}
$$

where the superscript $\{I,\lambda\}$ indicates that we move the nucleus I in the reference cell $\vec{L} = \vec{0}$ along the Cartesian direction λ. For the positions $R_I^{\vec{L}} = R_I^{\vec{0}} + \vec{L}$ holds. Note that derivatives are generally formed in the limit of a vanishing perturbation [128,129]. The nuclear repulsion term $E_{\mathrm{NN}}^{I,\lambda}$ asso-

ciated with $V_{\text{NN}}^{\vec{L}}$ is trivial and the same as in the nonrelativistic limit and the 1c methodology. According to Pulay, none of the derivatives include a response of the density matrix [130]. This finding holds for both DFT and Hartree-Fock theory based on converged 1c or 2c SCF procedures [131]. Instead of such an explicit response, the energy-weighted density matrix W arises for the first term given by

$$
E_{\text{T}}^{I,\lambda} = \sum_{\mu\nu} \sum_{\vec{L}} \left(T_{\mu\nu}^{\vec{L}} \right)^{I,\lambda} \left[\text{Re}\left(D_{\nu\mu}^{\alpha\alpha,\vec{L}} \right) + \text{Re}\left(D_{\nu\mu}^{\beta\beta,\vec{L}} \right) \right]
$$
$$
- \sum_{\mu\nu} \sum_{\vec{L}} \left(S_{\mu\nu}^{\vec{L}} \right)^{I,\lambda} \left[\text{Re}\left(W_{\nu\mu}^{\alpha\alpha,\vec{L}} \right) + \text{Re}\left(W_{\nu\mu}^{\beta\beta,\vec{L}} \right) \right]. \quad (69)
$$

Here, the energy-weighted density matrix is defined as

$$
W_{\mu\nu}^{\sigma\sigma',\vec{L}} = \frac{1}{V_{\text{FBZ}}} \sum_{i=1}^{n} \int_{\text{FBZ}}^{\epsilon_i^{\vec{k}} < \epsilon_{\text{F}}} e^{i\vec{k}\cdot\vec{L}} \left(c_{\mu i}^{\sigma,\vec{k}} \, \epsilon_i^{\vec{k}} \, c_{\nu i}^{*\sigma',\vec{k}} \right) d^3 k, \quad (70)
$$

which only differs from the density matrix by the inclusion of the spinor energy $\epsilon_i^{\vec{k}}$ in the integral [cf. Eq. (19)]. Owing to the properties of the overlap matrix, we only need the real part of the diagonal spin blocks, i.e., $\sigma = \sigma'$, which is the analog of the particle density matrix. Therefore, this term can be implemented straightforwardly based on the 1c routines.

The derivative of the Coulomb energy $E_{\text{J}}^{I,\lambda}$ does not depend on the spin-vector density but only on the particle density. Therefore, its derivative is the same as in the 1c formalism. Thus, it consists of a crystal-near-field and a crystal-far-field contribution

$$
E_{\text{J}}^{I,\lambda} = E_{\text{J,CNF}}^{I,\lambda} + E_{\text{J,CFF}}^{I,\lambda}. \quad (71)
$$

They are defined in Ref. [110], and we point to this reference for details.

For the spin-orbit ECPs, the derivative $E_{\text{SO}}^{I,\lambda}$ follows similarly to the kinetic energy contribution, and can be expressed as

$$
E_{\text{SO}}^{I,\lambda} = \sum_{\mu\nu} \sum_{\vec{L}} \text{Tr}\left[\left(h_{\mu\nu}^{\text{SO},\vec{L}} \right)^{I,\lambda} D_{\nu\mu}^{\vec{L}} \right]. \quad (72)
$$

Consequently, the one-electron SO-ECP integral derivatives are simply contracted with the antisymmetric linear combinations of the complex AO density matrix. These are the same as for the SCF energy calculation.

Finally, the derivative of the exchange-correlation energy $E_{\text{XC}}^{I,\lambda}$ is needed. Again, no derivative of the density matrix arises for first-order derivatives. Therefore, we only need to form the derivative of the XC potential matrix

$$
\left(X_{\mu\nu}^{\vec{L}} \right)^{I,\lambda} = \left(\int \xi_\mu^{\vec{0}}(\vec{r}) \, V^{\text{XC}}(\vec{r}) \, \xi_\nu^{\vec{L}}(\vec{r}) d^3 r \right)^{I,\lambda}. \quad (73)
$$

That is, the derivatives of $X_{\mu\nu}^{0,\vec{L}}$ and $X_{\mu\nu}^{u,\vec{L}}$ from Eqs. (41) and (42) (with $u \in \{x, y, z\}$) are calculated and contracted directly with the respective density matrices to yield $E_{\text{XC}}^{I,\lambda}$. These derivatives are now essentially given by the gradient of a product of Gaussian basis functions and the existing functional ingredients for SCF energies (cf. Refs. [132,133]). Weight derivatives for the numerical integration of the XC part are included based on the 2c generalization of previous work [108,110,123]. For closed-shell systems, the Kramers

restriction and time-reversal symmetry can be exploited as done for SCF energies. This way, the 2c Kramers-restricted implementation with semilocal functionals is almost completely available from an existing 1c implementation.

C. Stress tensor

Unit-cell parameters are optimized with the stress tensor [123,126,127] according to

$$
\frac{\partial E_{\text{SCF}}}{\partial v_{n,p}} = \sum_{q=\{x,y,z\}} \left[V_{\text{UC}} \, \sigma_{pq} - \sum_I \frac{\partial E_{\text{SCF}}}{\partial R_{I,p}} R_{I,q} \right] (A^{-1})_{nq}, \quad (74)
$$

where A is a (3×3) matrix consisting of the three vectors $\vec{v}_n$ describing the unit cell of a three-dimensional periodic system and $p, q \in \{x, y, z\}$ are the Cartesian components. The stress tensor components are given by

$$
\sigma_{pq} = \frac{1}{V_{\text{UC}}} \frac{\partial E_{\text{SCF}}}{\partial \epsilon_{pq}} \quad (75)
$$

with the volume of the unit cell V_{UC} and the symmetric strain tensor ϵ_{pq}. The latter describes the change of an atomic position $\vec{R}_I$ in a direct lattice cell $\vec{L}$ for an elastic deformation, i.e.,

$$
\left(R_{I,p}^{\vec{L}} \right)' = \sum_{q=\{x,y,z\}} (\delta_{pq} + \epsilon_{pq}) R_{I,q}^{\vec{L}} \quad (76)
$$

with the Kronecker delta δ_{pq}. The stress tensor follows as a sum over UC contributions

$$
\sigma_{pq} = \frac{1}{V_{\text{UC}}} \sum_{\vec{L}} \sum_I \frac{\partial E_{\text{SCF}}}{\partial R_{I,p}^{\vec{L}}} R_{I,q}^{\vec{L}} \quad (77)
$$

and the derivatives are obtained using Eq. (68). This leads to

$$
\sigma_{pq} = \frac{1}{V_{\text{UC}}} \sum_{\vec{L}} \sum_I \left[\frac{\partial E_{\text{T}}}{\partial R_{I,p}^{\vec{L}}} + \frac{\partial E_{\text{J}}}{\partial R_{I,p}^{\vec{L}}} + \frac{\partial E_{\text{NN}}}{\partial R_{I,p}^{\vec{L}}} \right] R_{I,q}^{\vec{L}}
$$
$$
+ \frac{1}{V_{\text{UC}}} \sum_{\vec{L}} \sum_I \left[\frac{\partial E_{\text{SO}}}{\partial R_{I,p}^{\vec{L}}} + \frac{\partial E_{\text{XC}}}{\partial R_{I,p}^{\vec{L}}} \right] R_{I,q}^{\vec{L}}, \quad (78)
$$

where the kinetic energy term again includes the energy-weighted density matrix

$$
\frac{\partial E_{\text{T}}}{\partial R_{I,p}^{\vec{L}}} = \sum_{\mu\nu} \sum_{\vec{L}'} \frac{\partial T_{\mu\nu}^{\vec{L}'}}{\partial R_{I,p}^{\vec{L}}} \left[\text{Re}\left(D_{\nu\mu}^{\alpha\alpha,\vec{L}'} \right) + \text{Re}\left(D_{\nu\mu}^{\beta\beta,\vec{L}'} \right) \right]
$$
$$
- \sum_{\mu\nu} \sum_{\vec{L}'} \frac{\partial S_{\mu\nu}^{\vec{L}'}}{\partial R_{I,p}^{\vec{L}}} \left[\text{Re}\left(W_{\nu\mu}^{\alpha\alpha,\vec{L}'} \right) + \text{Re}\left(W_{\nu\mu}^{\beta\beta,\vec{L}'} \right) \right]. \quad (79)
$$

Hence, the calculation of the stress tensor contributions essentially reduces to the calculation of derivatives with respect to nuclear displacements.

The Coulomb contribution is evaluated like in the nonrelativistic or scalar 1c limit [123], whereas the calculation of the SO-ECP and XC terms in Eq. (78) requires the additional AO density matrix linear combinations.

The derivatives of E_{SO} use the antisymmetric linear combinations $\text{Im}(D_{\nu\mu}^{\alpha\beta,\vec{L}'}) + \text{Im}(D_{\nu\mu}^{\beta\alpha,\vec{L}'})$, $\text{Re}(D_{\nu\mu}^{\alpha\beta,\vec{L}'}) - \text{Re}(D_{\nu\mu}^{\beta\alpha,\vec{L}'})$, and $\text{Im}(D_{\nu\mu}^{\alpha\alpha,\vec{L}'}) - \text{Im}(D_{\nu\mu}^{\beta\beta,\vec{L}'})$ for the contraction

with $\partial h_{\mu\nu}^{\mathrm{SO},u,\bar{L}'}/\partial R_{I,p}^{\bar{L}}$, with u denoting the spin-orbit components x, y, z.

For the XC contribution, the respective derivatives of $X_{\mu\nu}^{0,\bar{L}'}$ and $X_{\mu\nu}^{u,\bar{L}'}$ are contracted with the symmetric AO density matrices $\mathrm{Re}(D_{\nu\mu}^{\alpha\alpha,\bar{L}'}) + \mathrm{Re}(D_{\nu\mu}^{\beta\beta,\bar{L}'})$ for the scalar contributions, and $\mathrm{Re}(D_{\nu\mu}^{\alpha\beta,\bar{L}'}) + \mathrm{Re}(D_{\nu\mu}^{\beta\alpha,\bar{L}'})$, $\mathrm{Im}(D_{\nu\mu}^{\alpha\beta,\bar{L}'}) - \mathrm{Im}(D_{\nu\mu}^{\beta\alpha,\bar{L}'})$, and $\mathrm{Re}(D_{\nu\mu}^{\alpha\alpha,\bar{L}'}) - \mathrm{Re}(D_{\nu\mu}^{\beta\beta,\bar{L}'})$ for the noncollinear x, y, and z components. The evaluation of the derivatives of the XC potential ingredients ($\partial f^{\mathrm{XC}}/\partial\rho$, ξ_μ, etc.) is done as described in Refs. [117,123,134,135]. We emphasize that weight derivatives of the DFT part are of great importance for the stress tensor [134,136] and, therefore, we always include them based on Refs. [117,135].

D. Implementation

Due to the integral evaluation in real space, our implementation is largely based on the existing molecular implementations [43–45]. That is, the SO-ECP integrals are evaluated with the McMurchie-Davidson scheme [137,138]. All one- and two-electron integral routines are parallelized with the OPENMP paradigm [139,140]. Algebraic operations make use of the Math Kernel Library (MKL). Depending on the size of the basis set and the number of k points in reciprocal space, parallelization is either done over the k points or for the algebraic operations and transformations inside the loop over k points. The first option is used with many k points and comparably small basis sets, whereas the second option is used for large basis sets with more than, e.g., 5000 bands. The direct inversion in the iterative subspace (DIIS) is exploited to accelerate the SCF convergence [141] in its Γ-point version. Interfaces to LIBXC [142–144] are provided to support (almost) all semilocal density functional approximations. Both the canonical and the (modified) Scalmani-Frisch noncollinear formalism were implemented. The latter was also added for the molecular parts of the program suite, i.e., DFT energies [43,44,145], gradients [44,146], electron paramagnetic resonance properties [79,80], and the Green's function GW approach [91,147–149]. Global and range-separated hybrid functionals are available for the SCF procedure.

Our implementation supports the SCF initial construction of the band structure based on a discrete Hückel guess, core Hamiltonian guess, (noncollinear) superposition of atomic densities, converged 1c molecular orbitals (MOs), 2c molecular spinors, or 1c bands. The Kramers-restricted framework can only be used on top of MOs or bands of an RKS calculation. For the KU formalism, the starting wave function can be constructed as an eigenfunction of the spin operators $\hat{S}_x$, $\hat{S}_y$, or $\hat{S}_z$. For simplicity, we use the last option as default setting. By default, a threshold of 10^{-6} is used for the eigenvalues of the overlap matrix in the transformation to an orthogonal basis for periodic systems [150].

The 2c geometry gradients and the related stress tensor were implemented based on the 1c routines [110,123]. The SO-ECP integral derivatives are currently evaluated numerically (cf. the molecular implementation in Ref. [44]). The other contributions use analytical integral derivatives. All integral derivatives are parallelized with the OPENMP scheme.

Structures can be optimized with Grimme's DFT dispersion correction D3 [115], including Becke-Johnson (D3-BJ) damping [116].

E. SCF computation times

Table I shows the computation time for a three-dimensional face-centered-cubic (fcc) Pb crystal (primitive unit cell vectors' length 3.500 Å), employing 1c restricted Kohn-Sham (RKS), 1c UKS, 2c GKS KR, and 2c GKS KU frameworks. Here, we used the singlet state as initial guess since this is the ground state in 2c calculations. The number of atoms per unit cell is one, the number of k points used is 32 768 and the chosen grid size for the exchange-correlation potential is 4 [153,154]. Note that all frameworks except for 2c GKS KU use time-reversal symmetry for the k points. The PBE functional [151] was combined with the dhf-TZVP-2c orbital and auxiliary basis set [152]. Thus, small-core Dirac-Fock ECPs are applied (ECP-60) [155]. SCF thresholds of 10^{-8} hartree for the energy are chosen. Gaussian smearing is used with a criterion of 0.005 hartree. For comparison, the initial bands are obtained from a standard 1c Hückel guess.

The extension from a 1c to a 2c formalism has a crucial impact on the running time of the SCF procedure, due to the complex nature of the SCF orbitals in real space. This covers the following major steps.

(i) *Construction of the density matrix.* For the 2c KU formalism, the particle density ρ_{p} and the spin densities ρ_{m}^x, ρ_{m}^y, and ρ_{m}^z have to be constructed for both $+\vec{k}$ and $-\vec{k}$. Additionally, the densities for the contraction with the SO-ECP part are needed. Formally, this leads to a factor of 8, however, several densities can be processed simultaneously and symmetric and antisymmetric linear combinations are formed. In the KR framework, time-reversal symmetry is used as done for the 1c approaches. Thus, only half the number of k points is needed and the computation time is reduced.

(ii) *Coulomb matrix.* There is no structural change and no increase of the computation time.

(iii) *Exchange-correlation matrix.* For the 2c KU formalism, it is necessary to evaluate four densities ρ_{p}, ρ_{m}^x, ρ_{m}^y, and ρ_{m}^z on the DFT grid. Compared to the 1c RKS procedure, this leads to a factor of 4, or a factor of 2 compared to the 1c UKS procedure. The 2c KR approach does not lead to any extra costs relative to the 1c RKS ansatz.

(iv) *Diagonalization of the Kohn-Sham-Fock matrix.* For periodic systems, a single diagonalization of the Kohn-Sham-Fock matrix is eight times more involved compared to a 1c RKS calculation, as the dimensionality of matrices doubles due to the 2c construction. As the computational time scales as cubically with the number of basis functions, N_{BF}^3, this leads to the observed prefactor. In UKS theory, the spin components of the Kohn-Sham-Fock matrix can be decoupled, which is not possible in 2c GKS due to spin-orbit interaction.

The time investment needed for the diagonalization of the Kohn-Sham-Fock matrix depends on two factors, i.e., on the number of basis functions N_{BF} and the total number of k points N_k, as one diagonalization per k point is executed. This means that the computational costs of the diagonalization are proportional to N_{BF}^3 and to N_k. For smaller systems in terms of basis

TABLE I. Computation time in seconds for the SCF steps and number of iterations for a calculation of a three-dimensional Pb crystal (PBE functional [151], dhf-TZVP-2c basis [152]) with a single thread of an Intel Xeon Gold 6212U central processing unit @ 2.40 GHz. The number of atoms per unit cell is one, the number of k points is 32 768 and the chosen grid size for the XC potential is 4 [153,154]. The code was compiled with the Intel Fortran Compiler 19.0.1.144 (no just-in-time flags). The SCF initial guess is obtained by constructing bands from Hückel theory. The overlap, kinetic energy, ECP, and SO-ECP integrals are evaluated prior to entering the SCF iterations ("Pre-SCF"). Timings for the overlap and kinetic energy matrix are omitted, as they are negligible. "$D_{\mu\nu}$ build" refers to the construction of the density matrices in real space, "J" to the evaluation of the Coulomb integrals, and "XC" to the numerical integration of the XC potential. "Diag" and "Iter" denote the diagonalization for the Kohn-Sham equations and the number of iterations. "Time" denotes the computation time per iteration of the SCF procedure. Note that the energy contributions from the Coulomb term J and the XC part are again calculated after the last iteration. Bands are stored in binary format, while the MOs or spinors of the unit cell are stored in ASCII format (Band/MO dump) after converging the SCF procedure ("Post-SCF"). "Total" refers to the complete computation time.

	Pre-SCF		SCF						Post-SCF	
	ECP	SO-ECP	$D_{\mu\nu}$ build	J	XC	Diag	Time	Iter	Dump	Total
1c RKS	4.7	–	12.3	33.8	38.4	20.1	108.8	14	53.0	1656.4
1c UKS	4.9	–	24.7	33.8	50.6	39.6	156.7	14	104.6	2488.2
2c GKS KR	4.7	38.0	49.4	33.5	37.9	82.7	214.3	14	150.2	3253.5
2c GKS KU	4.9	38.4	96.9	33.6	90.4	231.3	483.9	14	301.7	7050.8

functions, the diagonalization time plays only a minor role for the total computation time. Ultimately, it is obvious that the diagonalization time for the 2c calculations is substantially larger than for the 1c calculations.

We conclude that for periodic systems, the 2c formalism provides an efficient way of dealing with physics based on spin-orbit coupling. To reduce the computational costs, the unit-cell size can be decreased to the minimum extent, while simultaneously increasing the number of k points in order to retain the same effective system size. This way, a linear increase of the computational demands proportional to N_k rather than the cubic proportionality of N_{BF}^3 is exploited. That allows us to perform calculations on large systems in a reasonable amount of time with standard computer hardware. Note that this statement is not only true for 2c periodic calculations but for periodic calculations in general.

III. APPLICATIONS TO DISCRETE AND PERIODIC SYSTEMS

In this section, we present calculations of various systems to illustrate applications of the 2c GTO-based approach and to show differences of the electronic structure by the inclusion of spin-orbit coupling. First, we discuss discrete atoms and subsequently systems that are periodic in three to one dimensions. Computational details are discussed in each subsection.

A. Ionization energies of zero-dimensional heavy p-block atoms

To begin with, we validate the implementation in the RIPER module of TURBOMOLE by comparison to the existing 2c molecular functionalities in the RIDFT module [43,44,156–158]. We study the ionization energies of heavy p elements. Compared to lighter elements, the ionization energies of heavy 5p and 6p elements follow a different trend. While the light elements show an increasing ionization energy from left to right in the periodic table with especially stable half-filled subshells [159,160], this is not the case for the heavy elements as they feature a heavier core and, therefore, stronger spin-orbit coupling. Strong spin-orbit coupling is accompanied by

a larger splitting of p, d, and f orbitals. Here, the splitting of the p shell is of particular importance. The p shells split into twofold-degenerated $p_{1/2}$ and fourfold-degenerated $p_{3/2}$ orbitals, indicating a stable p^2 configuration for lead. Thus, the ground state of lead is a triplet based on 1c calculations, while it is a singlet in 2c approaches.

According to the results in Table II, the computed ionization energies validate this trend. For all calculations, the PBE [151] (grid size 4 [153,154]) and PBE0 [161] exchange-correlation functionals combined with the dhf-SVP-2c GTO basis set [152] with small-core Dirac-Fock ECPs [155] are employed. The 2c procedure shows a good qualitative agreement with the experimental values, while the 1c calculations

TABLE II. Ionization energies based on energy differences of the atom and its cation for the heavy p-block elements In-I and Tl-At. The PBE [151] and PBE0 [161] exchange-correlation functionals combined with the dhf-SVP-2c Gaussian basis set [152] and small-core Dirac-Fock ECPs [155] are employed. Experimentally determined ionization potentials ("Experiment") are taken from Ref. [162]. All values are given in eV.

5p block	In	Sn	Sb	Te	I
1c RIPER PBE	5.58	7.26	8.95	8.66	10.42
2c RIPER PBE	5.70	7.14	8.67	8.86	10.31
2c RIDFT PBE	5.70	7.14	8.67	8.86	10.31
1c RIPER PBE0	5.61	7.31	9.05	8.68	10.55
2c RIPER PBE0	5.75	7.18	8.76	8.88	10.37
2c RIDFT PBE0	5.75	7.18	8.76	8.88	10.37
Experiment	5.70	7.34	8.64	9.01	10.45
6p block	Tl	Pb	Bi	Po	At
1c RIPER PBE	5.41	6.97	8.55	8.26	9.99
2c RIPER PBE	6.06	7.12	7.26	8.32	9.16
2c RIDFT PBE	6.06	7.12	7.26	8.32	9.16
1c RIPER PBE0	5.43	7.01	8.65	8.25	9.99
2c RIPER PBE0	6.10	7.15	7.33	8.36	9.20
2c RIDFT PBE0	6.10	7.15	7.33	8.36	9.20
Experiment	6.11	7.42	7.29	8.43	9.54

exhibit partly large deviations. On quantitative considerations, the 2c PBE simulations yield an average deviation of 0.14 eV from the experimental values, while we find an average deviation of 0.39 eV for the 1c procedure. PBE0 yields similar overall errors, as it does not consistently improve the results. Calculations with the RIDFT module lead to the same values as the RIPER module, demonstrating consistency.

B. Band structures of three-dimensional gold and lead crystals

Next, we demonstrate consistency of our implementation with well-established codes such as the plane-wave QUANTUM ESPRESSO program [52]. Therefore, we study the band structures of three-dimensional gold and lead crystals. Figure 1 shows the simulated electronic band structure for bulk gold and lead, forming a face-centered-cubic (fcc) lattice with a lattice constant of $a = 4.0800$ and 4.9508 Å, respectively [163].

For the RIPER calculations (1c, 2c), the PBE functional [151] (grid size 4) and the dhf-TZVP-2c GTO basis set [152] with small-core Dirac-Fock ECPs [155,164] (ECP-60 for Au and Pb) are employed. A k-point mesh of $32 \times 32 \times 32$ is used in combination with a Gaussian smearing of 0.005 hartree [165] to ensure convergence. Total SCF energies are converged up to 10^{-8} hartree. For the QUANTUM ESPRESSO calculations, we use the relativistic pseudopotentials Au.rel-pbe-dn-rrkjus_psl.0.1.UPF for gold and Pb.rel-pbe-dn-rrkjus_psl.0.2.2.UPF for lead, respectively. Cutoff radii of 100 hartree for the wave function and 1000 hartree for the electron density are set, while the other parameters such as the number of k points, the Gaussian smearing, and the convergence threshold are the same as for the RIPER calculations to ensure comparability.

The impact of spin-orbit interaction on the band structure of gold can be quantified by comparing 1c (orange) and 2c (purple) RIPER band structures in Fig. 1(a). We find that the influence of spin-orbit interaction is of minor relevance for bulk gold. For large parts of the electronic band structure, both curves are in excellent agreement, especially close to the Fermi level at $\epsilon_F = 0$ eV. The most prominent deviations between 1c and 2c calculations occur for band splittings at about 5.5 eV for the W point and at around -5 eV for the Γ point. The comparison of the band structure of the 2c RIPER (purple) and the QUANTUM ESPRESSO (red) calculations reveals a good agreement of energies below and around the Fermi level $\epsilon_F = 0$ eV. This indicates consistent results of the 2c RIPER implementation and the plane-wave QUANTUM ESPRESSO code, while providing the reduced calculation times of GTO over plane-wave basis sets. However, the band structures exhibit larger deviations in the region above 7 eV. This is not surprising as plane-wave basis sets are known to be superior in the description of energy states in the continuum above the gold work function, which amounts to around 5 eV [166].

In contrast to gold, the band structure of lead in Fig. 1(b) reveals a more pronounced impact of spin-orbit coupling due to the heavier atoms. Comparison of 1c (orange) and 2c (purple) RIPER band structures shows a band splitting of 0.87 eV at the W point for the energetic region around -1.5 eV. That is, the proper description of bulk electronic structures of heavy
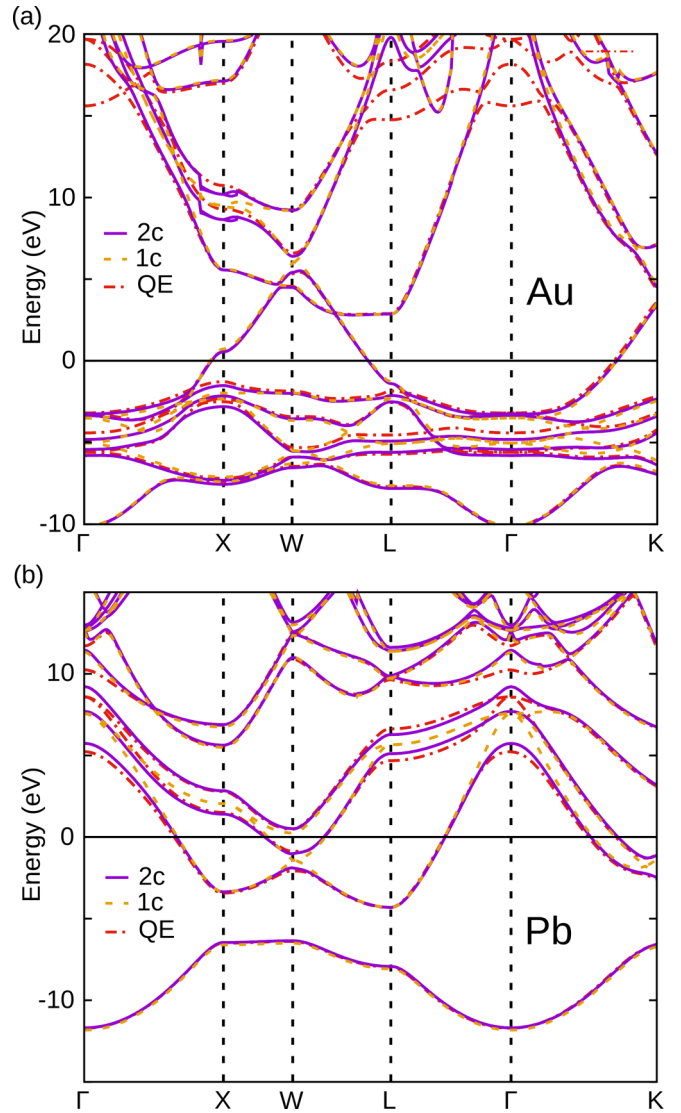

FIG. 1. Simulated band structure for (a) an fcc bulk gold crystal (lattice constant $a = 4.0800$ Å [163]) and (b) an fcc bulk lead crystal ($a = 4.9508$ Å [163]). Results for the RIPER module with (2c) and without (1c) spin-orbit coupling are shown together with relativistic 2c calculations using the QUANTUM ESPRESSO (QE) code [52]. All computations employ the PBE exchange-correlation functional [151]. We use the dhf-TZVP-2c GTO basis set for RIPER and a plane-wave basis for QUANTUM ESPRESSO. Vertical dashed lines mark high-symmetry points of the FBZ.

p-block systems generally necessitates the consideration of spin-orbit interaction. Figure 1(b) furthermore shows a similar behavior concerning the quality of our implementation for bulk lead. For energies below and around the Fermi level $\epsilon_F = 0$ eV, the band structures of both the relativistic QUANTUM ESPRESSO (red) and the 2c RIPER (purple) calculations match almost perfectly. In contrast, deviations are observed for energies above 5 eV. Again, this is a consequence of the better description of high-energy states close to the continuum with plane-wave basis sets (cf. the work function of Pb amounts to around 4 eV [167]).

TABLE III. Band gaps (in eV) of three-dimensional AgCl, AgBr, and AgI crystals (lattice constants $a = 5.612$, 5.843, and 6.169 Å, all rocksalt structure) at high-symmetry points of the FBZ with the PBE functional [151] and grid size 4. Nonrelativistic calculations (NR) are performed with the TZVPalls2 (Ag) [173], def2-TZVP (Cl, Br) [174], and the TZVPall (I) basis sets [173], whereas the ECP-based 1c and 2c calculations use the dhf-SVP bases [152] and small-core Dirac-Fock ECPs for Ag and I [175,176]. Results with scalar relativistic (SR) and spin-orbit (SO) X2c employing (truncated) Slater-type bases are taken from Ref. [169]. Four-component DKS results are taken from Ref. [170], employing uncontracted double-ζ basis sets [177–179].

AgCl	L-L	Γ-Γ	X-X	L-Γ
NR	4.86	3.72	5.32	1.66
1c ECP	4.62	3.11	4.16	0.91
SV ECP	4.57	2.94	3.99	0.86
2c ECP	4.57	2.94	3.99	0.86
SR X2c	4.31	3.09	4.23	0.92
SO X2c	4.27	2.99	4.03	0.88
4c DKS	4.47	2.93	4.20	0.87

AgBr	L-L	Γ-Γ	X-X	L-Γ
NR	4.28	3.19	4.77	1.56
1c ECP	4.07	2.64	3.70	0.86
SV ECP	4.02	2.64	3.54	0.82
2c ECP	4.02	2.64	3.54	0.82
SR X2c	3.87	2.43	3.87	0.68
SO X2c	3.77	2.25	3.67	0.60
4c DKS	3.82	2.24	3.68	0.61

AgI	L-L	Γ-Γ	X-X	L-X
NR	3.89	3.42	3.71	1.48
1c ECP	3.49	2.16	2.98	0.65
SV ECP	3.25	1.82	2.69	0.41
2c ECP	3.25	1.82	2.69	0.41
SR X2c	3.42	2.27	3.07	0.74
SO X2c	3.17	1.90	2.76	0.49
4c DKS	3.25	1.88	2.74	0.49

C. Band gaps of three-dimensional silver halide crystals

Silver halide crystals AgX ($X = $ Cl, Br, I) are typical model systems to study relativistic effects [168–171]. Studies have been performed with relativistic all-electron and ECP-based or quasirelativistic Hamiltonians. Due to the small gaps and the densely packed crystal structures, the systems are a challenging case for computational simulations [170]. In Table III, we compare results with our ECP-based implementation to previously reported ones from relativistic all-electron approaches including all-electron exact two-component (X2c) theory [169] and the four-component (4c) Dirac-Kohn-Sham (DKS) ansatz directly based on the many-electron Dirac-Coulomb equation [170]. Additionally, we used a non-self-consistent second-variational-like (SV) approach for SO effects [172]. Technically, the converged 1c bands are taken as initial guess for a 2c calculation and only one 2c diagonalization is carried out. For these calculations, the damping was turned off. We note that in the terminology of Ref. [172] we use $N_{\text{states}} = N_{\text{basis}}$ and these authors would

call our procedure a non-self-consistent first-variational approach.

Computational settings are chosen in accordance with previous studies [168–170]. Lattice constants are taken from Ref. [168], i.e., $a = 5.612$ Å for AgCl, $a = 5.843$ Å for AgBr, and $a = 6.169$ Å for AgI. Calculations are carried out with the primitive unit cell and a k mesh of $7 \times 7 \times 7$ points. Increasing this to $12 \times 12 \times 12$ changed the energy of AgCl by less than 3×10^{-6} hartree. SCF convergence thresholds are set to 10^{-7} hartree. Nonrelativistic calculations are performed with the TZVPalls2 (Ag), def2-TZVP [174] (Cl, Br), and the TZVPall (I) all-electron basis sets [173]. Scalar-relativistic and spin-orbit calculations employ the dhf-SVP basis sets [152] together with small-core Dirac-Fock ECPs (ECP-28) [175,176]. Note that we always transform the Kohn-Sham-Fock matrices into an orthogonal basis by diagonalization of the overlap matrix [threshold 10^{-6} (cf. Sec. II D)] [109]. Thus, we have not removed diffuse functions, i.e., functions with exponents smaller than 0.1 bohrs^{-1}, in contrast to related studies of silver halide crystals [168,169].

We find that the nonrelativistic framework is clearly insufficient for all systems, as it leads to a large deviation from the formally superior 4c DKS approach. Relativistic effects are mainly captured by scalar ECPs, i.e., the spatial contraction of the electron density is the leading relativistic correction. However, some band gaps such as the Γ-Γ and the X-X gap of AgI require the inclusion of spin-orbit coupling, as it lowers the gap by 0.2 eV. Likewise, the Γ-Γ and X-X gaps of AgCl and AgBr are notably affected. The SV and 2c-ECP approaches lead to the same band gaps for the considered semilocal functionals. The same holds for total energies. This finding is in line with the literature [172]. The SV approach is not sufficient for hybrid functionals which include the current density in the two-electron part (see below and Ref. [180]).

The 2c-ECP approach leads to a good agreement with relativistic all-electron X2c and DKS schemes. The qualitative trends of the band gaps are well described, and the 2c approach generally reduces the deviation towards the 4c DKS results. Exceptions in this regard are the X-X gaps of AgCl and AgBr. The same holds for scalar-relativistic and spin-orbit X2c calculations of the X-X gap of AgCl (see Refs. [169,170]). For both ECPs and X2c, spin-orbit effects lower these band gaps by about 0.2 eV. Therefore, considering these effects worsens the results, which hints at subtle error cancellation.

For comparison, we study the impact of the basis set and the density functional approximation. For the DFT study, we consider the first three rungs of Jacob's ladder [189]. The local spin density approximation (LSDA) is represented by the S-VWN (V) functional [190,191], whereas PBE [151] and PBEsol [192] serve as examples for GGAs. mGGAs are included with the TPSS [105], revTPSS [193,194], Tao-Mo [195], PKZB [196], and r^{2}SCAN [197,198] approximations. Note that we use LIBXC [142–144] for the PBEsol, revTPSS, Tao-Mo, PKZB, and r^{2}SCAN functionals. The dhf-SVP and dhf-TZVP basis sets are employed with fixed crystal structures, and results are listed in the Supplemental Material [199]. In addition, cell structure optimizations with these exchange-correlation functionals were carried out with the dhf-SVP basis [152,200], including the D3 correction with

TABLE IV. Optimized lattice constants a (in Å, rocksalt structure) of three-dimensional AgCl, AgBr, and AgI crystals and band gaps (in eV) at high-symmetry points of the FBZ with various density functional approximations and the dhf-SVP basis sets [152]. Experimental data taken from Refs. [181–188], as collected in Ref. [169].

AgCl		a	L-L	Γ-Γ	X-X	L-Γ
S-VWN (V)	no D3	5.377	3.93	3.27	3.85	0.55
PBE	no D3	5.624	4.58	2.91	3.99	0.86
PBEsol	no D3	5.515	4.20	2.98	3.89	0.66
TPSS	no D3	5.586	4.55	3.04	4.13	0.97
revTPSS	no D3	5.561	4.38	3.02	4.13	0.89
Tao-Mo	no D3	5.541	4.24	3.10	4.24	0.97
PKZB	no D3	5.636	4.59	3.10	4.26	1.18
r^{2}SCAN	no D3	5.576	5.02	3.55	4.56	1.41
PBE	D3-BJ	5.537	4.47	3.08	4.03	0.85
PBEsol	D3-BJ	5.426	4.07	3.20	3.93	0.66
TPSS	D3-BJ	5.498	4.40	3.21	4.18	0.94
revTPSS	D3-BJ	5.476	4.23	3.20	4.17	0.87
Tao-Mo	D3-BJ	5.511	4.20	3.17	4.25	0.97
r^{2}SCAN	D3-BJ	5.517	4.94	3.68	4.59	1.42
Experiment		5.550	–	5.2	–	3.0
AgBr		a	L-L	Γ-Γ	X-X	L-Γ
S-VWN (V)	no D3	5.604	3.42	2.82	3.39	0.54
PBE	no D3	5.849	4.03	2.63	3.54	0.82
PBEsol	no D3	5.692	3.60	2.77	3.45	0.65
TPSS	no D3	5.812	3.99	2.90	3.68	0.95
revTPSS	no D3	5.784	3.87	2.96	3.67	0.94
Tao-Mo	no D3	5.738	3.78	3.14	3.79	1.08
PKZB	no D3	5.868	4.13	2.99	3.81	1.19
r^{2}SCAN	no D3	5.811	4.50	3.36	4.09	1.42
PBE	D3-BJ	5.747	3.89	2.82	3.57	0.83
PBEsol	D3-BJ	5.613	3.48	2.95	3.48	0.67
TPSS	D3-BJ	5.708	3.82	3.09	3.71	0.95
revTPSS	D3-BJ	5.690	3.72	3.14	3.70	0.94
Tao-Mo	D3-BJ	5.743	3.79	3.13	3.79	1.08
r^{2}SCAN	D3-BJ	5.772	4.45	3.44	4.10	1.42
Experiment		5.774	–	4.3	–	2.5
AgI		a	L-L	Γ-Γ	X-X	L-X
S-VWN (V)	no D3	5.937	2.73	1.96	2.70	-0.17
PBE	no D3	6.187	3.27	1.79	2.67	0.44
PBEsol	no D3	6.023	2.88	1.93	2.74	0.09
TPSS	no D3	6.153	3.25	2.05	2.94	0.58
revTPSS	no D3	6.116	3.15	2.13	3.00	0.54
Tao–Mo	no D3	6.071	3.10	2.34	3.11	0.62
PKZB	no D3	6.200	3.41	2.15	2.99	0.83
r^{2}SCAN	no D3	6.159	3.78	2.50	3.24	0.91
PBE	D3-BJ	6.067	3.11	1.99	2.78	0.28
PBEsol	D3-BJ	5.927	2.74	2.12	2.84	-0.06
TPSS	D3-BJ	5.982	2.99	2.35	3.10	0.34
revTPSS	D3-BJ	5.949	2.88	2.44	3.16	0.29
Tao–Mo	D3-BJ	6.068	3.10	2.35	3.11	0.61
r^{2}SCAN	D3-BJ	6.156	3.77	2.51	3.24	0.91
Experiment		6.067	–	–	–	–

Becke-Johnson damping if available [76,115,116,201,202]. All other computational parameters such as SCF thresholds and grids are unchanged, compared to the Hamiltonian study

in Table III. The main results are listed in Table IV (see Supplemental Material [199] for all results).

Obviously, the impact of the density functional approximations is much larger than the deviations between the 2c ECP and the all-electron X2c or DKS ansatz. Especially for the small L-Γ and L-X band gaps, the choice of the semilocal functional substantially affects the results. Here, the gaps increase from LSDA to GGA functionals and tend to further rise for the mGGAs. This finding also holds for the other band gaps of all AgX systems. For AgI, the L-X band gap is very small and negative gaps are obtained at the S-VWN (V) and PBEsol-D3 levels. Negative L-X band gaps of AgI were already found by the group of Liu with S-VWN [169].

Dispersion correction leads to notably decreased lattice constants and thus indirectly affects the band gaps. For the lattice constants, the PBE-D3 functional performs best for AgCl, whereas r^{2}SCAN-D3 and Tao-Mo-D3 perform best for AgBr and AgI, respectively.

According to the Supplemental Material [199], the larger triple-ζ basis sets consistently lower the gaps, which is in agreement with similar studies at the DKS level [170].

We note, however, that none of the semilocal density functionals applied herein are able to accurately reproduce the experimental band gaps for AgCl and AgBr. Therefore, we study the performance of the range-separated hybrid functionals HSE03 [203,204], HSE06 [203–205], HSEsol [206], and HSE12 [207] using LIBXC [142–144]. Computational settings are unchanged except that the threshold for the canonical orthogonalization was raised from 10^{-6} to 5.5×10^{-5} for AgCl with all hybrid functionals and for AgBr with HSE12 in order to facilitate the SCF convergence. This removes three vectors for AgCl with all hybrid functionals and also three vectors for AgBr with HSE12. For AgI, the smallest eigenvalue of the overlap matrix is larger than 10^{-3}, ensuring a smooth convergence. Results are listed in Table V.

Admixture of Fock exchange substantially increases the band gaps and hence improves the agreement with experiment. Especially, the L-Γ gap rises and the silver halides become small-gap semiconductors in line with the experimental findings. The impact of the proper 2c generalization using the spin-current density for Fock exchange is comparably small for these systems.

In conclusion, an ECP-based implementation is sufficient for the band gaps of crystals, as this property is driven by the valence region. In contrast, all-electron approaches may be needed for other properties or for a fully parameter-free description of relativistic effects.

D. Indium(I,III)-telluride two-dimensional honeycomb system

To illustrate the applicability of the implementation to two-dimensional systems, we consider the indium(I,III)-telluride (InTe) honeycomb crystal displayed in Fig. 2(a). For layered two-dimensional materials and their atomically thin layers dispersion interaction may play an important role. Here, we use the PBE functional [151] (grid size 4) combined with the D3-BJ correction [115,116]. The dhf-TZVP-2c basis set [152] is applied, and a k mesh of 32×32 is employed. A Gaussian smearing of 0.001 hartree [165] and an SCF threshold of 10^{-8} hartree are chosen. The cell structure is optimized with the 2c
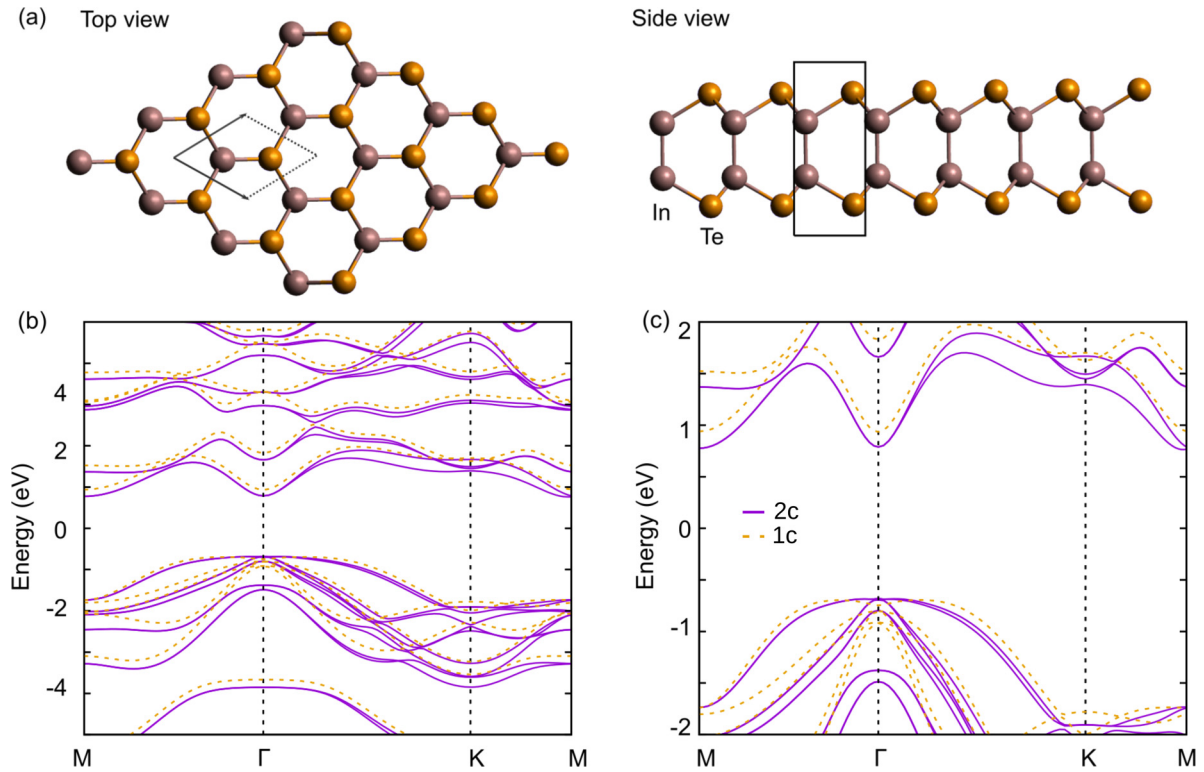
FIG. 2. (a) Top and side views of the two-dimensional InTe honeycomb system with indicated unit cell. The unit cell consists of two In and two Te atoms. (b), (c) Electronic band structure of the FBZ. The orange dashed lines are calculated without spin-orbit coupling, while the solid purple lines include spin-orbit interaction. The black vertical dashed lines mark the Γ and K points of the Brillouin zone. Calculations are performed with the PBE functional [151], the D3-BJ dispersion correction [115,116], and the dhf-TZVP-2c basis set [152]. See Supplemental Material [199] for results with HSE06 [203–205].

Hamiltonian, and band structures are shown in Figs. 2(b) and 2(c). For comparison, the electronic band structure based on the unit-cell structure optimized without the D3-BJ correction and spin-orbit interaction is displayed in the Supplemental Material [199].

We find that dispersion correction and weight derivatives are important for the unit-cell structure and consequently the band gap. Without D3-BJ and weight derivatives, an in-plane lattice constant of 4.17 Å, and band gaps of 1.56 eV (1c) and 1.12 eV (2c) are obtained. Adding the D3-BJ correction and weight derivatives changes the lattice constant to 4.23 Å. Band gaps are increased to 1.63 eV (1c) and 1.44 eV (2c). This reveals a delicate interplay of spin-orbit coupling and cell structure.

The most notable changes of the band structure induced by spin-orbit coupling are found for the Γ point in the energetic region from 1 to 2 eV below the Fermi level of $\epsilon_F = 0$ eV. Here, the energies of the two occupied bands are substantially decreased. The shifts for these bands at about -1.5 eV amount to more than 0.5 eV.

The reduction of the bands gap from 1.63 to 1.44 eV due to spin-orbit coupling is mainly caused by the energetic decrease of the band 1 eV above the Fermi level. Overall, our results are in reasonable agreement with those of Shang *et al.* [208], who reported a band gap of 1.27 eV.

Application of Fock exchange using the HSE06 functional [203–205] with a k mesh of 17×17 and a threshold of 5.5×10^{-5} for the orthogonal basis increases the band gap

to 2.29 eV. Inclusion of spin-orbit coupling changes this to 2.13 eV without spin currents in the Fock exchange and to 2.09 eV with the complete 2c Fock exchange. According to the band plots in the Supplemental Material [199], the increase of the band gap for HSE06 compared to PBE is mainly due to the energetic shift of occupied bands.

E. One-dimensional platinum chains

Electron transport through atomically thin wires serves as a sensitive probe of their electronic structure. Scalar-relativistic effects have been pointed out to be crucial for the chain formation in metallic atomic contacts of Ir, Pt, and Au [209]. From these three elements, Pt and Ir have been suggested to show interesting magnetic effects based on the spin-orbit coupling, such as an anisotropic magnetoresistance [24]. As chains are pulled, they transition from a zigzag to a linear configuration [210]. While linear chains are thus not the ground-state geometry for all interatomic distances, linear chains of Pt are by now a reference system for a transition to a magnetic state [24,211–214]. We will reexamine this system with our implementation here.

Our unit cell consists of two platinum atoms and is indicated in Fig. 1(a). The cell parameter d was varied from 4.0 to 6.0 Å, with structures specified in the Supplemental Material [199]. For the calculations, the PBE exchange-correlation functional [151] (grid size 4 [153,154]) and the dhf-SVP-2c GTO basis set [152] with small-core Dirac-Fock ECPs [164]

TABLE V. Band gaps (in eV) of three-dimensional AgCl, AgBr, and AgI crystals (lattice constants $a = 5.612$, 5.843, and 6.169 Å, all rocksalt structure) at high-symmetry points of the FBZ with the PBE [151], HSE03 [203,204], HSE06 [203–205], HSEsol [206], and the HSE12 [207] functionals. "no j" and "j" denote that the spin current density contributions are neglected or included for the 2c Fock exchange. Only the latter option is the complete 2c generalization of the Fock exchange.

AgCl	L-L	Γ-Γ	X-X	L-Γ
1c PBE	4.62	3.11	4.16	0.91
2c PBE	4.57	2.94	3.99	0.86
1c HSE03	6.06	4.54	6.27	2.44
2c HSE03 (no j)	6.02	4.54	6.10	2.39
2c HSE03 (j)	6.01	4.54	6.09	2.39
1c HSE06	5.97	4.49	6.23	2.37
2c HSE06 (no j)	5.93	4.48	6.05	2.33
2c HSE06 (j)	5.93	4.48	6.05	2.33
1c HSEsol	5.81	4.42	6.15	2.26
2c HSEsol (no j)	5.76	4.41	5.97	2.22
2c HSEsol (j)	5.76	4.41	5.97	2.22
1c HSE12	6.42	4.95	6.87	2.86
2c HSE12 (no j)	6.37	4.94	6.70	2.81
2c HSE12 (j)	6.37	4.94	6.69	2.81
Experiment	–	5.2	–	3.0

AgBr	L-L	Γ-Γ	X-X	L-Γ
1c PBE	4.07	2.64	3.70	0.86
2c PBE	4.02	2.64	3.54	0.82
1c HSE03	5.34	3.88	5.60	2.23
2c HSE03 (no j)	5.30	3.87	5.54	2.19
2c HSE03 (j)	5.30	3.87	5.54	2.19
1c HSE06	5.25	3.83	5.58	2.17
2c HSE06 (no j)	5.21	3.82	5.50	2.13
2c HSE06 (j)	5.21	3.82	5.49	2.13
1c HSEsol	5.09	3.77	5.57	2.08
2c HSEsol (no j)	5.05	3.77	5.42	2.04
2c HSEsol (j)	5.05	3.76	5.41	2.04
1c HSE12	5.65	4.24	6.04	2.61
2c HSE12 (no j)	5.61	4.23	6.02	2.58
2c HSE12 (j)	5.61	4.23	6.02	2.58
Experiment	–	4.3	–	2.5

AgI	L-L	Γ-Γ	X-X	L-X
1c PBE	3.49	2.16	2.98	0.65
2c PBE	3.25	1.82	2.69	0.41
1c HSE03	4.54	3.22	4.06	1.76
2c HSE03 (no j)	4.27	2.87	3.77	1.50
2c HSE03 (j)	4.24	2.84	3.75	1.47
1c HSE06	4.45	3.18	4.04	1.73
2c HSE06 (no j)	4.19	2.83	3.75	1.47
2c HSE06 (j)	4.16	2.80	3.73	1.44
1c HSEsol	4.31	3.12	4.06	1.70
2c HSEsol (no j)	4.05	2.78	3.77	1.44
2c HSEsol (j)	4.02	2.74	3.74	1.41
1c HSE12	4.79	3.54	4.43	2.11
2c HSE12 (no j)	4.52	3.19	4.14	1.85
2c HSE12 (j)	4.48	3.15	4.10	1.81
Experiment	–	–	–	–

are employed. 32 k points are used in combination with a Gaussian smearing of 0.01 hartree [165]. SCF procedures are converged with a threshold of 10^{-8} hartree. We started the SCF calculations both from a closed-shell initial guess and an open-shell initial guess based on four unpaired electrons. In the 2c calculations, the initial wave function is chosen to be an eigenfunction of S_x or S_z, and the converged 2c wave function is thus aligned accordingly. We also confirmed the settings for the 2c calculations using a superposition of atomic densities with the magnetization aligned along the x or z axis for both Pt atoms as initial guess. Note that we assume periodicity along the x direction for one-dimensional systems [150]. Results with the Scalmani-Frisch approach are further listed in the Supplemental Material [199].

According to the restricted and unrestricted DFT calculations in Figs. 3(d)–3(f), no notable spin polarization occurs for unit cells with d smaller than 5.0 Å. Here, the spin expectation values are essentially zero. The most energetically favorable geometric structure is found for $d = 4.75$ Å in both scalar-relativistic and spin-orbit calculations. Apparently the impact of spin-orbit coupling on the geometric structure is small for this system. However, spin-orbit interaction has a large impact on the electronic band structure. For the 2c Kramers-restricted solution in Fig. 3(a), only two bands cross the Fermi level at $\epsilon_F = 0$ eV. In contrast, seven and four bands cross the Fermi level for the Kramers-unrestricted solutions with S_x and S_z alignments, respectively [see Figs. 3(b) and 3(c)]. For the latter two cases, many bands are split due to spin-orbit effects. Thus, we find that spin-orbit interaction substantially affects the band structure for all spin configurations.

Furthermore, spin-orbit coupling is of relevance for the magnetic moment and the spin expectation value. The Pt chains transition into a magnetic state at $d = 5.25$ Å without taking spin-orbit interaction into account, while spin-orbit effects change the transition geometry to $d = 5.04$ Å for the S_x orientation and to $d = 5.35$ Å for the S_z orientation. For the absolute spin expectation values, we find $\langle S_z \rangle = 1.2$ for large $d = 6.0$ Å in the 1c UKS formalism, while the 2c calculations lead to $\langle S_x \rangle = 1.0$ and $\langle S_z \rangle = 0.85$. This corresponds to a large magnetic anisotropy as choosing the spin parallel to the periodic direction (x axis) notably affects the absolute spin expectation values and consequently the magnetic moments. In the spin-only approximation, the latter are obtained in units of Bohr's magneton μ_B by doubling the spin expectation value. Since our unit cell contains two atoms, the spin expectation values listed above directly correspond to the magnetic moments in μ_B per atom.

Changing the density functional approximation to the LSDA functional S-VWN (V) [190,191] or to the mGGA functional TPSS [105] leads to a transition geometry of $d = 5.3$ and 5.2 Å (1c). Inclusion of spin-orbit coupling results in a jump of the magnetization at $d = 5.0$ and 4.9 Å for the spin alignment parallel to the chain at the 2c level, respectively. The spin expectation value for large cells is very similar to the PBE result. The 1c UKS formalism predicts a jump of the magnetic moment at about $d = 5.1$ Å for both functionals. Notably, the range-separated hybrid functional HSE06 [203–205] leads to a transition already at $d = 4.7$ Å (1c). We refer to the Supplemental Material [199] for the complete results with S-VWN (V), TPSS, and HSE06.
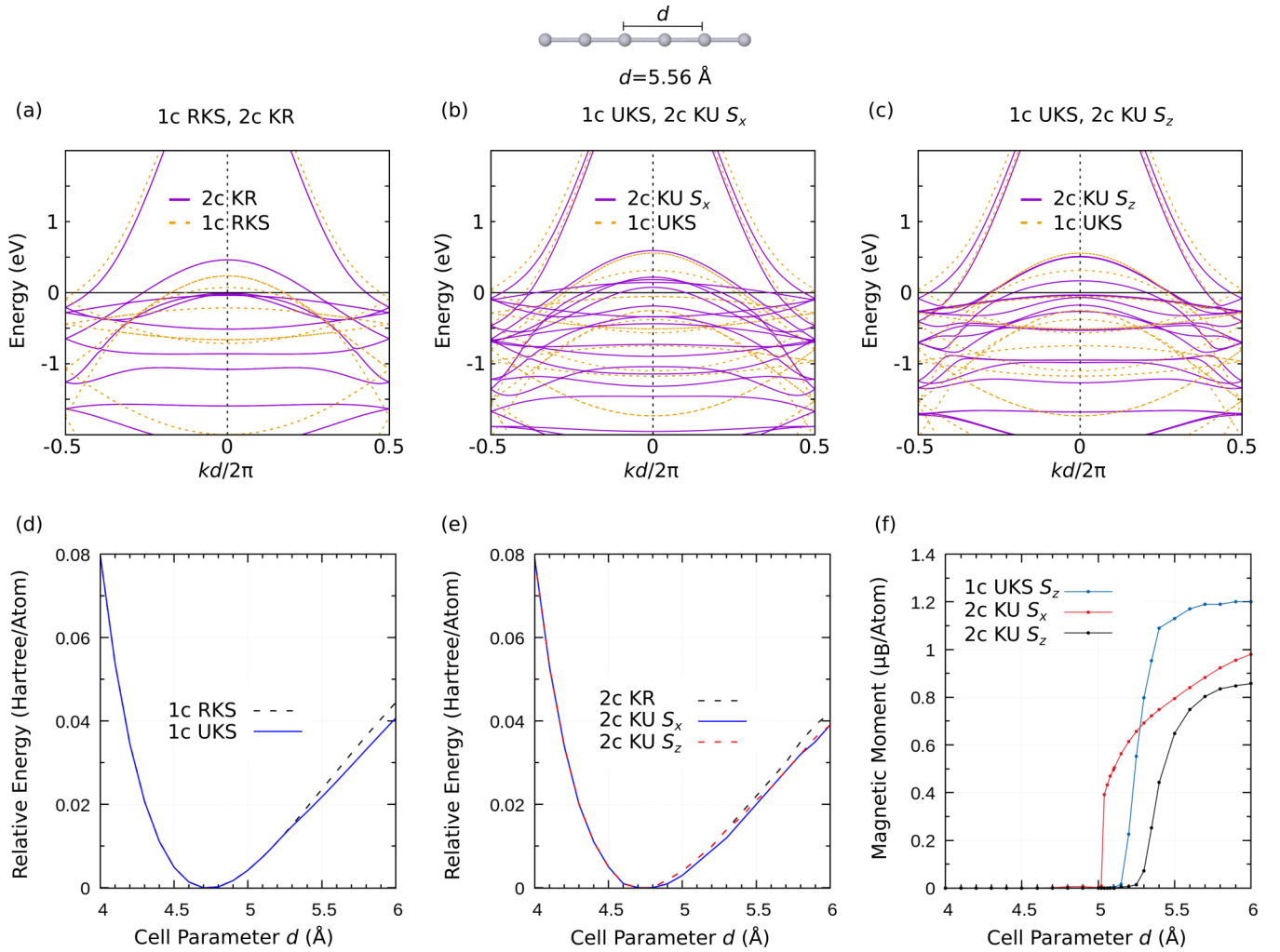
FIG. 3. (a)–(c) Electronic band structure in the FBZ for a linear platinum chain at $d = 5.56$ Å. The unit cell consists of two platinum atoms and is exemplarily shown above (b). The black vertical dashed lines in each panel mark the Γ point of the FBZ. Expectation values of the respective spin components are 1.16 [1c UKS, (b) and (c)], 0.82 [2c KU S_x, (b)], and 0.71 [2c KU S_z, (c)], and the spin vector is fully aligned along the x and z direction, respectively. Note that we assume periodicity along the x direction for one-dimensional systems [150]. The open-shell solutions are energetically favored compared to the respective closed-shell solutions (1c RKS or 2c KR) by about 4×10^{-3} hartree (1c UKS), 2×10^{-3} hartree (2c KU S_x alignment), and 10^{-3} hartree (2c KU S_z alignment). The magnetization parallel to the nanowire is thus energetically preferred to the perpendicular one by about 10^{-3} hartree. Calculations are performed with the PBE functional [151] and the dhf-SVP-2c basis set [152]. (d) Dependence of the energy on the cell parameter in units of hartree per atom for 1c RKS and 1c UKS. (e) Dependence of the energy on the cell parameter in units of hartree per atom for 2c KR, 2c KU S_x, and 2c KU S_z. (f) Magnetic moment in units of Bohr's magneton μ_B per atom for the spin contribution of 1c UKS, 2c KU S_x, and 2c KU S_z.

Our scalar-relativistic results are in excellent agreement with the study of Fernández-Rossier *et al.* [213], who predicted an equilibrium structure with $d = 4.8$ Å. Additionally, they observed the magnetic transition at $d = 5.2$ Å and a magnetic moment of 1.2 μ_B per atom at $d = 6.0$ Å based on 1c UKS PBE calculations with the GTO-based code CRYSTAL03. Note that these authors used one platinum atom per unit cell and hence the lattice spacing in their work has to be converted for comparison with our results.

Our results are also in qualitative agreement with the study of Smogunov *et al.* using plane-wave methods [214]. They obtained an equilibrium distance of $d_0 \approx 4.8$ Å (GGA), which is in close agreement with our prediction of $d_0 = 4.8$ Å. Additionally, the transition to a magnetic state occurs at smaller d values for a magnetization parallel to the chain than for

a perpendicular magnetization. A jump of the magnetic moment is found at $d \approx 4.84$ Å for the first orientation with GGA functionals and at slightly smaller d for LSDA. For the perpendicular magnetization, the jump is at $d \approx 5.2$ Å. Smogunov *et al.* [214] also found that the parallel magnetization is energetically favored, which is in agreement with our calculations.

IV. SUMMARY AND OUTLOOK

We presented an efficient two-component DFT procedure, which accounts for spin-orbit interaction as well as for scalar-relativistic effects. Relativistic effects are introduced with effective core potentials. Due to the use of atom-centered Gaussian-type orbitals, our implementation is applicable to

both molecular and periodic systems of any dimensionality. For ground-state energy calculations hybrid functionals are available to account for the self-consistent relaxation of the induced current density.

We demonstrated the validity of our approach by calculating the ionization energies of heavy p-block atoms, the electronic bulk band structure of gold and lead, band gaps of silver halide crystals, the geometry and band structure of the InTe honeycomb system, as well as the spin polarizations of linear platinum chains. In the process, we assessed the accuracy of the implementation by comparison with the plane-wave-based QUANTUM ESPRESSO program and other codes, showing excellent agreement.

Extension of this work is promising in multiple directions. In terms of density functional approximations, this covers the extension of the mGGA framework to account for the

current density as done in Ref. [45]. An extension to local hybrid functionals [215] may be useful to allow for a more flexible admixture of Fock exchange [216–218]. Additionally, relativistic all-electron approaches are necessary to study energetically low-lying states and the density in the vicinity of the nuclei [145,146].

[1] M. Dolg and X. Cao, Relativistic pseudopotentials: Their development and scope of applications, Chem. Rev. **112**, 403 (2012).

[2] T. Saue, Relativistic Hamiltonians for chemistry: A primer, ChemPhysChem **12**, 3077 (2011).

[3] J. Autschbach, Perspective: Relativistic effects, J. Chem. Phys. **136**, 150902 (2012).

[4] P. Pyykkö, Relativistic effects in chemistry: More common than you thought, Annu. Rev. Phys. Chem. **63**, 45 (2012).

[5] W. Liu, Essentials of relativistic quantum chemistry, J. Chem. Phys. **152**, 180901 (2020).

[6] K. G. Dyall and K. Fægri, Jr., *Introduction to Relativistic Quantum Chemistry* (Oxford University Press, New York, USA, 2007).

[7] M. Reiher and A. Wolf, *Relativistic Quantum Chemistry: The Fundamental Theory of Molecular Science*, 2nd ed. (Wiley-VCH, Weinheim, Germany, 2015).

[8] *Handbook of Relativistic Quantum Chemistry*, edited by W. Liu (Springer, Berlin, Germany, 2017).

[9] P. Pyykkö, The physics behind chemistry and the periodic table, Chem. Rev. **112**, 371 (2012).

[10] P. Schwerdtfeger, *Relativistic Electronic Structure Theory: Part 1. Fundamentals* (Elsevier, Amsterdam, The Netherlands, 2002).

[11] P. Schwerdtfeger, *Relativistic Electronic Structure Theory: Part 2. Applications* (Elsevier, Amsterdam, The Netherlands, 2004).

[12] S. Wilson, I. Grant, and B. L. Gyorffy, *The Effects of Relativity in Atoms, Molecules, and the Solid State* (Springer, New York, USA, 1991).

[13] I. Grant, Relativistic electronic structure of atoms and molecules, in *Advances in Atomic, Molecular, and Optical Physics*, edited by B. Bederson and A. Dalgarno (Academic, San Diego, USA, 1994), Vol. 32, pp. 169–186.

[14] P. Pyykkö, Theoretical chemistry of gold. III, Chem. Soc. Rev. **37**, 1967 (2008).

[15] P. Pyykko and J. P. Desclaux, Relativity and the periodic system of elements, Acc. Chem. Res. **12**, 276 (1979).

[16] P. Pyykko, Relativistic effects in structural chemistry, Chem. Rev. **88**, 563 (1988).

[17] Z. Li, Y. Xiao, and W. Liu, On the spin separation of algebraic two-component relativistic Hamiltonians, J. Chem. Phys. **137**, 154114 (2012).

[18] L. Cheng and J. Gauss, Perturbative treatment of spin-orbit coupling within spin-free exact two-component theory, J. Chem. Phys. **141**, 164107 (2014).

[19] L. Cheng, F. Wang, J. F. Stanton, and J. Gauss, Perturbative treatment of spin-orbit-coupling within spin-free exact two-component theory using equation-of-motion coupled-cluster methods, J. Chem. Phys. **148**, 044108 (2018).

[20] J. K. Desmarais, A. Erba, J.-P. Flament, and B. Kirtman, Perturbation theory treatment of spin–orbit coupling II: A coupled perturbed Kohn–Sham method, J. Chem. Theory Comput. **17**, 4712 (2021).

[21] K. Ishizaka, M. Bahramy, H. Murakawa, M. Sakano, T. Shimojima, T. Sonobe, K. Koizumi, S. Shin, H. Miyahara, A. Kimura, K. Miyamoto, T. Okuda, H. Namatame, M. Taniguchi, R. Rita, N. Nagaosa, K. Kobayashi, Y. Murakami, R. Kumai, Y. Kaneko *et al.*, Giant Rashba-type spin splitting in bulk BiTeI, Nat. Mater. **10**, 521 (2011).

[22] J. Kübler, *Theory of Itinerant Electron Magnetism* (Oxford University Press, New York, USA, 2000).

[23] D. Pesin and L. Balents, Mott physics and band topology in materials with strong spin–orbit interaction, Nat. Phys. **6**, 376 (2010).

[24] V. M. García-Suárez, D. Z. Manrique, C. J. Lambert, and J. Ferrer, Anisotropic magnetoresistance in atomic chains of iridium and platinum from first principles, Phys. Rev. B **79**, 060408(R) (2009).

[25] M. Häfner, J. K. Viljas, and J. C. Cuevas, Theory of anisotropic magnetoresistance in atomic-sized ferromagnetic metal contacts, Phys. Rev. B **79**, 140410(R) (2009).

[26] B. Hardrat, F. Freimuth, S. Heinze, and Y. Mokrousov, Conductance fingerprints of noncollinear magnetic states in single-atom contacts: A first-principles Wannier-functions study, Phys. Rev. B **86**, 165449 (2012).

[27] D. Jacob, J. Fernández-Rossier, and J. J. Palacios, Anisotropic magnetoresistance in nanocontacts, Phys. Rev. B **77**, 165412 (2008).

[28] S. Schmaus, A. Bagrets, Y. Nahas, T. K. Yamada, A. Bork, M. Bowen, E. Beaurepaire, F. Evers, and W. Wulfhekel,

Giant magnetoresistance through a single molecule, Nat. Nanotechnol. **6**, 185 (2011).

[29] S. L. Kawahara, J. Lagoute, V. Repain, C. Chacon, Y. Girard, S. Rousset, A. Smogunov, and C. Barreteau, Large magnetoresistance through a single molecule due to a spin-split hybridized orbital, Nano Lett. **12**, 4558 (2012).

[30] R. Hayakawa, M. A. Karimi, J. Wolf, T. Huhn, M. S. Zöllner, C. Herrmann, and E. Scheer, Large magnetoresistance in single-radical molecular junctions, Nano Lett. **16**, 4960 (2016).

[31] F. Strigl, C. Espy, M. Bückle, E. Scheer, and T. Pietsch, Emerging magnetic order in platinum atomic contacts and chains, Nat. Commun. **6**, 6172 (2015).

[32] D. Li, F. Pauly, and A. Smogunov, Giant anisotropic magnetoresistance through a tilted molecular π-orbital, Phys. Rev. Res. **2**, 033184 (2020).

[33] W. Kang, Y. Huang, X. Zhang, Y. Zhou, and W. Zhao, Skyrmion-electronics: An overview and outlook, Proc. IEEE **104**, 2040 (2016).

[34] M. Heide, G. Bihlmayer, and S. Blügel, Dzyaloshinskii-Moriya interaction accounting for the orientation of magnetic domains in ultrathin films: Fe/W(110), Phys. Rev. B **78**, 140403(R) (2008).

[35] M. Heide, G. Bihlmayer, and S. Blügel, Describing Dzyaloshinskii–Moriya spirals from first principles, Phys. B (Amsterdam) **404**, 2678 (2009).

[36] M. Z. Hasan and C. L. Kane, Colloquium: Topological insulators, Rev. Mod. Phys. **82**, 3045 (2010).

[37] C. Pauly, G. Bihlmayer, M. Liebmann, M. Grob, A. Georgi, D. Subramaniam, M. R. Scholz, J. Sánchez-Barriga, A. Varykhalov, S. Blügel, O. Rader, and M. Morgenstern, Probing two topological surface bands of Sb$_2$Te$_3$ by spin-polarized photoemission spectroscopy, Phys. Rev. B **86**, 235106 (2012).

[38] M. Dolg, Relativistic effective core potentials, in *Relativistic Electronic Structure Theory*, Theoretical and Computational Chemistry, edited by P. Schwerdtfeger (Elsevier, Amsterdam, The Netherlands, 2002), Vol. 11, Chap. 14, pp. 793–862.

[39] M. Dolg, Relativistic effective core potentials, in *Handbook of Relativistic Quantum Chemistry*, edited by W. Liu (Springer, Berlin, Germany, 2017), Chap. 14, pp. 449–478.

[40] J. Kubler, K.-H. Höck, J. Sticht, and A. R. Williams, Density functional theory of non-collinear magnetism, J. Phys. F: Met. Phys. **18**, 469 (1988).

[41] C. Van Wüllen, Relativistic all-electron density functional calculations, J. Comput. Chem. **20**, 51 (1999).

[42] C. Van Wüllen, Spin densities in two-component relativistic density functional calculations: Noncollinear versus collinear approach, J. Comput. Chem. **23**, 779 (2002).

[43] M. K. Armbruster, F. Weigend, C. van Wüllen, and W. Klopper, Self-consistent treatment of spin-orbit interactions with efficient Hartree-Fock and density functional methods, Phys. Chem. Chem. Phys. **10**, 1748 (2008).

[44] A. Baldes and F. Weigend, Efficient two-component self-consistent field procedures and gradients: implementation in TURBOMOLE and application to Au$_{20}^-$, Mol. Phys. **111**, 2617 (2013).

[45] C. Holzer, Y. J. Franzke, and A. Pausch, Current density functional framework for spin–orbit coupling, J. Chem. Phys. **157**, 204102 (2022).

[46] J. E. Peralta, G. E. Scuseria, and M. J. Frisch, Noncollinear magnetism in density functional calculations, Phys. Rev. B **75**, 125119 (2007).

[47] G. Scalmani and M. J. Frisch, A new approach to noncollinear spin density functional theory beyond the local density approximation, J. Chem. Theory Comput. **8**, 2193 (2012).

[48] I. W. Bulik, G. Scalmani, M. J. Frisch, and G. E. Scuseria, Noncollinear density functional theory having proper invariance and local torque properties, Phys. Rev. B **87**, 035117 (2013).

[49] J. K. Desmarais, S. Komorovsky, J.-P. Flament, and A. Erba, Spin–orbit coupling from a two-component self-consistent approach. II. Non-collinear density functional theories, J. Chem. Phys. **154**, 204110 (2021).

[50] J. K. Desmarais, J.-P. Flament, and A. Erba, Spin-orbit coupling in periodic systems with broken time-reversal symmetry: Formal and computational aspects, Phys. Rev. B **101**, 235142 (2020).

[51] C. D. Sherrill, D. E. Manolopoulos, T. J. Martínez, and A. Michaelides, Electronic structure software, J. Chem. Phys. **153**, 070401 (2020).

[52] P. Giannozzi, O. Baseggio, P. Bonfà, D. Brunato, R. Car, I. Carnimeo, C. Cavazzoni, S. de Gironcoli, P. Delugas, F. Ferrari Ruffino, A. Ferretti, N. Marzari, I. Timrov, A. Urru, and S. Baroni, QUANTUM ESPRESSO toward the exascale, J. Chem. Phys. **152**, 154105 (2020).

[53] P. Blaha, K. Schwarz, F. Tran, R. Laskowski, G. K. H. Madsen, and L. D. Marks, WIEN2k: An APW+lo program for calculating the properties of solids, J. Chem. Phys. **152**, 074101 (2020).

[54] A. García, N. Papior, A. Akhtar, E. Artacho, V. Blum, E. Bosoni, P. Brandimarte, M. Brandbyge, J. I. Cerdá, F. Corsetti, R. Cuadrado, V. Dikan, J. Ferrer, J. Gale, P. García-Fernández, V. M. García-Suárez, S. García, G. Huhs, S. Illera, R. Korytár *et al.*, SIESTA: Recent developments and applications, J. Chem. Phys. **152**, 204108 (2020).

[55] R. Dovesi, F. Pascale, B. Civalleri, K. Doll, N. M. Harrison, I. Bush, P. D'Arco, Y. Noël, M. Rérat, P. Carbonnière, M. Causà, S. Salustro, V. Lacivita, B. Kirtman, A. M. Ferrari, F. S. Gentile, J. Baima, M. Ferrero, R. Demichelis, and M. De La Pierre, The CRYSTAL code, 1976–2020 and beyond, a long story, J. Chem. Phys. **152**, 204111 (2020).

[56] T. D. Kühne, M. Iannuzzi, M. Del Ben, V. V. Rybkin, P. Seewald, F. Stein, T. Laino, R. Z. Khaliullin, O. Schütt, F. Schiffmann, D. Golze, J. Wilhelm, S. Chulkov, M. H. Bani-Hashemian, V. Weber, U. Borštnik, M. Taillefumier, A. S. Jakobovits, A. Lazzaro, H. Pabst *et al.*, CP2K: An electronic structure and molecular dynamics software package - Quickstep: Efficient and accurate electronic structure calculations, J. Chem. Phys. **152**, 194103 (2020).

[57] J. C. A. Prentice, J. Aarons, J. C. Womack, A. E. A. Allen, L. Andrinopoulos, L. Anton, R. A. Bell, A. Bhandari, G. A. Bramley, R. J. Charlton, R. J. Clements, D. J. Cole, G. Constantinescu, F. Corsetti, S. M.-M. Dubois, K. K. B. Duff, J. M. Escartín, A. Greco, Q. Hill, L. P. Lee *et al.*, The ONETEP linear-scaling density functional theory program, J. Chem. Phys. **152**, 174111 (2020).

[58] Q. Sun, X. Zhang, S. Banerjee, P. Bao, M. Barbry, N. S. Blunt, N. A. Bogdanov, G. H. Booth, J. Chen, Z.-H. Cui, J. J. Eriksen, Y. Gao, S. Guo, J. Hermann, M. R. Hermes, K. Koh, P. Koval,

S. Lehtola, Z. Li, J. Liu *et al.*, Recent developments in the PySCF program package, J. Chem. Phys. **153**, 024109 (2020).

[59] M. J. Frisch, G. W. Trucks, H. B. Schlegel, G. E. Scuseria, M. A. Robb, J. R. Cheeseman, G. Scalmani, V. Barone, G. A. Petersson, H. Nakatsuji, X. Li, M. Caricato, A. V. Marenich, J. Bloino, B. G. Janesko, R. Gomperts, B. Mennucci, H. P. Hratchian, J. V. Ortiz, A. F. Izmaylov *et al.*, Gaussian 16 Revision C.01 (Gaussian Inc. Wallingford, CT, USA, 2016).

[60] G. Kresse and J. Furthmüller, Efficient iterative schemes for *ab initio* total-energy calculations using a plane-wave basis set, Phys. Rev. B **54**, 11169 (1996).

[61] S. G. Balasubramani, G. P. Chen, S. Coriani, M. Diedenhofen, M. S. Frank, Y. J. Franzke, F. Furche, R. Grotjahn, M. E. Harding, C. Hättig, A. Hellweg, B. Helmich-Paris, C. Holzer, U. Huniar, M. Kaupp, A. Marefat Khah, S. Karbalaei Khani, T. Müller, F. Mack, B. D. Nguyen *et al.*, TURBOMOLE: Modular program suite for *ab initio* quantum-chemical and condensed-matter simulations, J. Chem. Phys. **152**, 184107 (2020).

[62] Developers' version of TURBOMOLE V7.7 (2022), a development of University of Karlsruhe and Forschungszentrum Karlsruhe GmbH, 1989-2007, TURBOMOLE GmbH, since 2007; available from https://www.turbomole.org.

[63] R. Ahlrichs, M. Bär, M. Häser, H. Horn, and C. Kölmel, Electronic structure calculations on workstation computers: The program system turbomole, Chem. Phys. Lett. **162**, 165 (1989).

[64] F. Furche, R. Ahlrichs, C. Hättig, W. Klopper, M. Sierka, and F. Weigend, Turbomole, Wiley Interdiscip. Rev.: Comput. Mol. Sci. **4**, 91 (2014).

[65] Y. J. Franzke, C. Holzer, J. H. Andersen, T. Begušić, F. Bruder, S. Coriani, F. Della Sala, E. Fabiano, D. A. Fedotov, S. Fürst, S. Gillhuber, R. Grotjahn, M. Kaupp, M. Kehry, M. Krstić, F. Mack, S. Majumdar, B. D. Nguyen, S. M. Parker, F. Pauly *et al.*, TURBOMOLE: Today and Tomorrow, J. Chem. Theory Comput. **19**, 6859 (2023).

[66] J. M. Kasper, A. J. Jenkins, S. Sun, and X. Li, Perspective on Kramers symmetry breaking and restoration in relativistic electronic structure methods for open-shell systems, J. Chem. Phys. **153**, 090903 (2020).

[67] J. K. Desmarais, J.-P. Flament, and A. Erba, Adiabatic connection in spin-current density functional theory, Phys. Rev. B **102**, 235118 (2020).

[68] F. Bodo, J. K. Desmarais, and A. Erba, Spin current density functional theory of Weyl semimetals, Phys. Rev. B **105**, 125108 (2022).

[69] A. Erba, J. K. Desmarais, S. Casassa, B. Civalleri, L. Donà, I. J. Bush, B. Searle, L. Maschio, L. Edith-Daga, A. Cossard, C. Ribaldone, E. Ascrizzi, N. L. Marana, J.-P. Flament, and B. Kirtman, CRYSTAL23: A program for computational solid state physics and chemistry, J. Chem. Theory Comput. **19**, 6891 (2023).

[70] Y. J. Franzke, W. M. Schosser, and F. Pauly, Efficient treatment of relativistic effects with periodic density functional methods: Energies, gradients, and stress tensors, arXiv:2305.03817.

[71] J. K. Desmarais, A. Erba, and J.-P. Flament, Structural relaxation of materials with spin-orbit coupling: Analytical forces in spin-current DFT, arXiv:2306.04309.

[72] J. K. Desmarais, A. Erba, and J.-P. Flament, Structural relaxation of materials with spin-orbit coupling: Analyti-

cal forces in spin-current DFT, Phys. Rev. B **108**, 134108 (2023).

[73] N. Mardirossian and M. Head-Gordon, Thirty years of density functional theory in computational chemistry: an overview and extensive assessment of 200 density functionals, Mol. Phys. **115**, 2315 (2017).

[74] P. Hao, J. Sun, B. Xiao, A. Ruzsinszky, G. I. Csonka, J. Tao, S. Glindmeyer, and J. P. Perdew, Performance of meta-GGA functionals on general main group thermochemistry, kinetics, and noncovalent interactions, J. Chem. Theory Comput. **9**, 355 (2013).

[75] Y. Mo, R. Car, V. N. Staroverov, G. E. Scuseria, and J. Tao, Assessment of the Tao-Mo nonempirical semilocal density functional in applications to solids and surfaces, Phys. Rev. B **95**, 035118 (2017).

[76] L. Goerigk, A. Hansen, C. Bauer, S. Ehrlich, A. Najibi, and S. Grimme, A look at the density functional theory zoo with the advanced GMTKN55 database for general main group thermochemistry, kinetics and noncovalent interactions, Phys. Chem. Chem. Phys. **19**, 32184 (2017).

[77] T. Aschebrock and S. Kümmel, Ultranonlocality and accurate band gaps from a meta-generalized gradient approximation, Phys. Rev. Res. **1**, 033082 (2019).

[78] C. Holzer, Y. J. Franzke, and M. Kehry, Assessing the accuracy of local hybrid density functional approximations for molecular response properties, J. Chem. Theory Comput. **17**, 2928 (2021).

[79] Y. J. Franzke and J. M. Yu, Hyperfine coupling constants in local exact two-component theory, J. Chem. Theory Comput. **18**, 323 (2022).

[80] Y. J. Franzke and J. M. Yu, Quasi-relativistic calculation of EPR *g* tensors with derivatives of the decoupling transformation, gauge-including atomic orbitals, and magnetic balance, J. Chem. Theory Comput. **18**, 2246 (2022).

[81] A. D. Becke, Perspective: Fifty years of density-functional theory in chemical physics, J. Chem. Phys. **140**, 18A301 (2014).

[82] A. D. Becke, Density-functional theory vs density-functional fits, J. Chem. Phys. **156**, 214101 (2022).

[83] P. Borlido, T. Aull, A. W. Huran, F. Tran, M. A. L. Marques, and S. Botti, Large-scale benchmark of exchange–correlation functionals for the determination of electronic band gaps of solids, J. Chem. Theory Comput. **15**, 5069 (2019).

[84] A. Ghosh, S. Jana, T. Rauch, F. Tran, M. A. L. Marques, S. Botti, L. A. Constantin, M. K. Niranjan, and P. Samal, Efficient and improved prediction of the band offsets at semiconductor heterojunctions from meta-GGA density functionals: A benchmark study, J. Chem. Phys. **157**, 124108 (2022).

[85] P. Kovács, F. Tran, P. Blaha, and G. K. H. Madsen, What is the optimal mGGA exchange functional for solids?, J. Chem. Phys. **157**, 094110 (2022).

[86] Y. J. Franzke and C. Holzer, Exact two-component theory becoming an efficient tool for NMR shieldings and shifts with spin–orbit coupling, J. Chem. Phys. **159**, 184102 (2023).

[87] J. F. Dobson, Alternative expressions for the Fermi hole curvature, J. Chem. Phys. **98**, 8870 (1993).

[88] A. D. Becke, Current density in exchange-correlation functionals: Application to atomic states, J. Chem. Phys. **117**, 6935 (2002).

[89] J. Tao, Explicit inclusion of paramagnetic current density in the exchange-correlation functionals of current-density functional theory, Phys. Rev. B **71**, 205107 (2005).

[90] J. E. Bates and F. Furche, Harnessing the meta-generalized gradient approximation for time-dependent density functional theory, J. Chem. Phys. **137**, 164105 (2012).

[91] Y. J. Franzke, C. Holzer, and F. Mack, NMR coupling constants based on the Bethe–Salpeter equation in the *GW* approximation, J. Chem. Theory Comput. **18**, 1030 (2022).

[92] Y. J. Franzke and C. Holzer, Impact of the current density on paramagnetic NMR properties, J. Chem. Phys. **157**, 031102 (2022).

[93] F. Bruder, Y. J. Franzke, and F. Weigend, Paramagnetic NMR shielding tensors based on scalar exact two-component and spin–orbit perturbation theory, J. Phys. Chem. A **126**, 5050 (2022).

[94] A. Pausch and C. Holzer, Linear response of current-dependent density functional approximations in magnetic fields, J. Phys. Chem. Lett. **13**, 4335 (2022).

[95] C. J. Schattenberg and M. Kaupp, Effect of the current dependence of tau-dependent exchange-correlation functionals on nuclear shielding calculations, J. Chem. Theory Comput. **17**, 1469 (2021).

[96] F. Bruder, Y. J. Franzke, C. Holzer, and F. Weigend, Zero-field splitting parameters within exact two-component theory and modern density functional theory using seminumerical integration, J. Chem. Phys. **159**, 194117 (2023).

[97] Y. J. Franzke, F. Bruder, S. Gillhuber, C. Holzer, and F. Weigend, Paramagnetic nuclear magnetic resonance shifts for triplet systems and beyond with modern relativistic density functional methods, J. Phys. Chem. A **128**, 670 (2024).

[98] E. I. Tellgren, A. M. Teale, J. W. Furness, K. K. Lange, U. Ekström, and T. Helgaker, Non-perturbative calculation of molecular magnetic properties within current-density functional theory, J. Chem. Phys. **140**, 034101 (2014).

[99] J. W. Furness, J. Verbeke, E. I. Tellgren, S. Stopkowicz, U. Ekström, T. Helgaker, and A. M. Teale, Current density functional theory using meta-generalized gradient exchange-correlation functionals, J. Chem. Theory Comput. **11**, 4169 (2015).

[100] S. Reimann, U. Ekström, S. Stopkowicz, A. M. Teale, A. Borgoo, and T. Helgaker, The importance of current contributions to shielding constants in density-functional theory, Phys. Chem. Chem. Phys. **17**, 18834 (2015).

[101] T. J. P. Irons, L. Spence, G. David, B. T. Speake, T. Helgaker, and A. M. Teale, Analyzing magnetically induced currents in molecular systems using current-density-functional theory, J. Phys. Chem. A **124**, 1321 (2020).

[102] S. Sen and E. I. Tellgren, Benchmarking density functional approximations for diamagnetic and paramagnetic molecules in nonuniform magnetic fields, J. Chem. Theory Comput. **17**, 1480 (2021).

[103] Y. Zhao and D. G. Truhlar, A new local density functional for main-group thermochemistry, transition metal bonding, thermochemical kinetics, and noncovalent interactions, J. Chem. Phys. **125**, 194101 (2006).

[104] Y. Zhao and D. G. Truhlar, The M06 suite of density functionals for main group thermochemistry, thermochemical kinetics, noncovalent interactions, excited states, and transition ele-

ments: two new functionals and systematic testing of four M06-class functionals and 12 other functionals, Theor. Chem. Acc. **120**, 215 (2008).

[105] J. Tao, J. P. Perdew, V. N. Staroverov, and G. E. Scuseria, Climbing the density functional ladder: Nonempirical meta–generalized gradient approximation designed for molecules and solids, Phys. Rev. Lett. **91**, 146401 (2003).

[106] R. Grotjahn, F. Furche, and M. Kaupp, Importance of imposing gauge invariance in time-dependent density functional theory calculations with meta-generalized gradient approximations, J. Chem. Phys. **157**, 111102 (2022).

[107] A. M. Burow, M. Sierka, and F. Mohamed, Resolution of identity approximation for the Coulomb term in molecular and periodic systems, J. Chem. Phys. **131**, 214101 (2009).

[108] A. M. Burow and M. Sierka, Linear scaling hierarchical integration scheme for the exchange-correlation term in molecular and periodic systems, J. Chem. Theory Comput. **7**, 3097 (2011).

[109] R. Łazarski, A. M. Burow, and M. Sierka, Density functional theory for molecular and periodic systems using density fitting and continuous fast multipole methods, J. Chem. Theory Comput. **11**, 3029 (2015).

[110] R. Łazarski, A. M. Burow, L. Grajciar, and M. Sierka, Density functional theory for molecular and periodic systems using density fitting and continuous fast multipole method: Analytical gradients, J. Comput. Chem. **37**, 2518 (2016).

[111] L. Grajciar, Low-memory iterative density fitting, J. Comput. Chem. **36**, 1521 (2015).

[112] A. Irmler, A. M. Burow, and F. Pauly, Robust periodic Fock exchange with atom-centered Gaussian basis sets, J. Chem. Theory Comput. **14**, 4567 (2018).

[113] A. Irmler and F. Pauly, Multipole-based distance-dependent screening of Coulomb integrals, J. Chem. Phys. **151**, 084111 (2019).

[114] F. Egidi, S. Sun, J. J. Goings, G. Scalmani, M. J. Frisch, and X. Li, Two-component noncollinear time-dependent spin density functional theory for excited state calculations, J. Chem. Theory Comput. **13**, 2591 (2017).

[115] S. Grimme, J. Antony, S. Ehrlich, and H. Krieg, A consistent and accurate *ab initio* parametrization of density functional dispersion correction (DFT-D) for the 94 elements H-Pu, J. Chem. Phys. **132**, 154104 (2010).

[116] S. Grimme, S. Ehrlich, and L. Goerigk, Effect of the damping function in dispersion corrected density functional theory, J. Comput. Chem. **32**, 1456 (2011).

[117] P. M. Gill, B. G. Johnson, and J. A. Pople, A standard grid for density functional calculations, Chem. Phys. Lett. **209**, 506 (1993).

[118] G. I. Csonka, J. P. Perdew, and A. Ruzsinszky, Global hybrid functionals: A look at the engine under the hood, J. Chem. Theory Comput. **6**, 3688 (2010).

[119] P. W. Gill, R. D. Adamson, and J. A. Pople, Coulomb-attenuated exchange energy density functionals, Mol. Phys. **88**, 1005 (1996).

[120] T. Leininger, H. Stoll, H.-J. Werner, and A. Savin, Combining long-range configuration interaction with short-range density functionals, Chem. Phys. Lett. **275**, 151 (1997).

[121] T. Yanai, D. P. Tew, and N. C. Handy, A new hybrid exchange–correlation functional using the Coulomb-attenuating method (CAM-B3LYP), Chem. Phys. Lett. **393**, 51 (2004).

[122] T. M. Henderson, B. G. Janesko, and G. E. Scuseria, Range separation and local hybridization in density functional theory, J. Phys. Chem. A **112**, 12530 (2008).

[123] M. Becker and M. Sierka, Density functional theory for molecular and periodic systems using density fitting and continuous fast multipole method: Stress tensor, J. Comput. Chem. **40**, 2563 (2019).

[124] K. N. Kudin and G. E. Scuseria, Analytic stress tensor with the periodic fast multipole method, Phys. Rev. B **61**, 5141 (2000).

[125] T. Bučko, J. Hafner, and J. G. Ángyán, Geometry optimization of periodic systems using internal coordinates, J. Chem. Phys. **122**, 124508 (2005).

[126] K. Doll, Analytical stress tensor and pressure calculations with the CRYSTAL code, Mol. Phys. **108**, 223 (2010).

[127] F. Knuth, C. Carbogno, V. Atalla, V. Blum, and M. Scheffler, All-electron formalism for total energy strain derivatives and stress tensor components for numeric atom-centered orbitals, Comput. Phys. Commun. **190**, 33 (2015).

[128] H. B. Schlegel, Geometry optimization, Wiley Interdiscip. Rev.: Comput. Mol. Sci. **1**, 790 (2011).

[129] P. Pulay, Analytical derivatives, forces, force constants, molecular geometries, and related response properties in electronic structure theory, Wiley Interdiscip. Rev.: Comput. Mol. Sci. **4**, 169 (2014).

[130] P. Pulay, *Ab initio* calculation of force constants and equilibrium geometries in polyatomic molecules, Mol. Phys. **17**, 197 (1969).

[131] L. Versluis and T. Ziegler, The determination of molecular structures by density functional theory. The evaluation of analytical energy gradients by numerical integration, J. Chem. Phys. **88**, 322 (1988).

[132] J. A. Pople, P. M. Gill, and B. G. Johnson, Kohn–Sham density-functional theory within a finite basis set, Chem. Phys. Lett. **199**, 557 (1992).

[133] B. G. Johnson, P. M. W. Gill, and J. A. Pople, The performance of a family of density functional methods, J. Chem. Phys. **98**, 5612 (1993).

[134] J. Baker, J. Andzelm, A. Scheiner, and B. Delley, The effect of grid quality and weight derivatives in density functional calculations, J. Chem. Phys. **101**, 8894 (1994).

[135] R. Stratmann, G. E. Scuseria, and M. J. Frisch, Achieving linear scaling in exchange-correlation density functional quadratures, Chem. Phys. **257**, 213 (1996).

[136] M. Tobita, S. Hirata, and R. J. Bartlett, The analytical energy gradient scheme in the Gaussian based Hartree–Fock and density functional theory for two-dimensional systems using the fast multipole method, J. Chem. Phys. **118**, 5776 (2003).

[137] L. E. McMurchie and E. R. Davidson, Calculation of integrals over *ab initio* pseudopotentials, J. Comput. Phys. **44**, 289 (1981).

[138] R. M. Pitzer and N. W. Winter, Spin-orbit (core) and core potential integrals, Int. J. Quantum Chem. **40**, 773 (1991).

[139] OpenMP Architecture Review Boards, OpenMP API shared-memory parallel programming, https://www.openmp.org, accessed on December 20, 2022.

[140] C. Holzer and Y. J. Franzke, OpenMP versions of RIDFT, RDGRAD, and EGRAD with contributions to MPSHIFT, DSCF, and GRAD; improved OpenMP versions of AOFORCE and ESCF, released with TURBOMOLE V7.4 and further improved in TURBOMOLE V7.5.

[141] P. Pulay, Convergence acceleration of iterative sequences. The case of SCF iteration, Chem. Phys. Lett. **73**, 393 (1980).

[142] M. A. L. Marques, M. J. T. Oliveira, and T. Burnus, LIBXC: A library of exchange and correlation functionals for density functional theory, Comput. Phys. Commun. **183**, 2272 (2012).

[143] S. Lehtola, C. Steigemann, M. J. T. Oliveira, and M. A. L. Marques, Recent developments in LIBXC– a comprehensive library of functionals for density functional theory, SoftwareX **7**, 1 (2018).

[144] LIBXC, Version 6.0.0, https://www.tddft.org/programs/libxc/, accessed on August 16, 2022.

[145] D. Peng, N. Middendorf, F. Weigend, and M. Reiher, An efficient implementation of two-component relativistic exact-decoupling methods for large molecules, J. Chem. Phys. **138**, 184105 (2013).

[146] Y. J. Franzke, N. Middendorf, and F. Weigend, Efficient implementation of one- and two-component analytical energy gradients in exact two-component theory, J. Chem. Phys. **148**, 104110 (2018).

[147] M. Kehry, Y. J. Franzke, C. Holzer, and W. Klopper, Quasirelativistic two-component core excitations and polarisabilities from a damped-response formulation of the Bethe–Salpeter equation, Mol. Phys. **118**, e1755064 (2020).

[148] C. Holzer and W. Klopper, Ionized, electron-attached, and excited states of molecular systems with spin–orbit coupling: Two-component GW and Bethe–Salpeter implementations, J. Chem. Phys. **150**, 204116 (2019).

[149] C. Holzer, Practical post-Kohn–Sham methods for time-reversal symmetry breaking references, J. Chem. Theory Comput. **19**, 3131 (2023).

[150] Manual of TURBOMOLE V7.7 (2022), a development of University of Karlsruhe and Forschungszentrum Karlsruhe GmbH, 1989-2007, TURBOMOLE GmbH, since 2007; available from https://www.turbomole.org/turbomole/turbomole-documentation/.

[151] J. P. Perdew, K. Burke, and M. Ernzerhof, Generalized gradient approximation made simple, Phys. Rev. Lett. **77**, 3865 (1996).

[152] F. Weigend and A. Baldes, Segmented contracted basis sets for one- and two-component Dirac–Fock effective core potentials, J. Chem. Phys. **133**, 174102 (2010).

[153] O. Treutler, Entwicklung und Anwendung von Dichtefunktionalmethoden, Dissertation (Dr. rer. nat.), University of Karlsruhe (TH), Germany, 1995, https://publikationen.bibliothek.kit.edu/12796.

[154] O. Treutler and R. Ahlrichs, Efficient molecular numerical integration schemes, J. Chem. Phys. **102**, 346 (1995).

[155] B. Metz, H. Stoll, and M. Dolg, Small-core multiconfiguration-Dirac–Hartree–Fock-adjusted pseudopotentials for post-*d* main group elements: Application to PbH and PbO, J. Chem. Phys. **113**, 2563 (2000).

[156] K. Eichkorn, O. Treutler, H. Öhm, M. Häser, and R. Ahlrichs, Auxiliary basis sets to approximate coulomb potentials, Chem. Phys. Lett. **240**, 283 (1995).

[157] K. Eichkorn, F. Weigend, O. Treutler, and R. Ahlrichs, Auxiliary basis sets for main row atoms and transition metals and their use to approximate Coulomb potentials, Theor. Chem. Acc. **97**, 119 (1997).

[158] F. Weigend, M. Kattannek, and R. Ahlrichs, Approximated electron repulsion integrals: Cholesky decomposition versus resolution of the identity methods, J. Chem. Phys. **130**, 164106 (2009).

[159] J. E. Huheey, E. A. Keiter, and R. L. Keiter, *Inorganic Chemistry: Principles of Structure and Reactivity*, 4th ed. (HarperCollins, New York, USA, 1994).

[160] C. E. Housecroft and A. G. Sharpe, *Inorganic Chemistry*, 4th ed. (Pearson, Harlow, United Kingdom, 2012).

[161] C. Adamo and V. Barone, Toward reliable density functional methods without adjustable parameters: The PBE0 model, J. Chem. Phys. **110**, 6158 (1999).

[162] Y. Ralchenko, F. Jou, D. Kelleher, A. Kramida, A. Musgrove, J. Reader, W. Wiese, and K. Olsen, NIST atomic spectra database (version 3.1.0) (2006), accessed on March 27, 2023, http://physics.nist.gov/asd3.

[163] WolframResearch, ElementData, https://reference.wolfram.com/language/ref/ElementData.html, accessed on December 2, 2021.

[164] D. Figgen, K. A. Peterson, M. Dolg, and H. Stoll, Energy-consistent pseudopotentials and correlation consistent basis sets for the 5d elements Hf–Pt, J. Chem. Phys. **130**, 164108 (2009).

[165] G. Kresse and J. Furthmüller, Efficiency of *ab-initio* total energy calculations for metals and semiconductors using a plane-wave basis set, Comput. Mater. Sci. **6**, 15 (1996).

[166] W. Sachtler, G. Dorgelo, and A. Holscher, The work function of gold, Surf. Sci. **5**, 221 (1966).

[167] P. A. Anderson and A. L. Hunt, Work function of lead, Phys. Rev. **102**, 367 (1956).

[168] J. E. Peralta, J. Uddin, and G. E. Scuseria, Scalar relativistic all-electron density functional calculations on periodic systems, J. Chem. Phys. **122**, 084108 (2005).

[169] R. Zhao, Y. Zhang, Y. Xiao, and W. Liu, Exact two-component relativistic energy band theory and application, J. Chem. Phys. **144**, 044105 (2016).

[170] M. Kadek, M. Repisky, and K. Ruud, All-electron fully relativistic Kohn–Sham theory for solids based on the Dirac–Coulomb Hamiltonian and Gaussian-type functions, Phys. Rev. B **99**, 205103 (2019).

[171] C.-N. Yeh, A. Shee, Q. Sun, E. Gull, and D. Zgid, Relativistic self-consistent *GW*: Exact two-component formalism with one-electron approximation for solids, Phys. Rev. B **106**, 085121 (2022).

[172] W. P. Huhn and V. Blum, One-hundred-three compound band-structure benchmark of post-self-consistent spin-orbit coupling treatments in density functional theory, Phys. Rev. Mater. **1**, 033803 (2017).

[173] R. Ahlrichs and K. May, Contracted all-electron Gaussian basis sets for atoms Rb to Xe, Phys. Chem. Chem. Phys. **2**, 943 (2000).

[174] F. Weigend and R. Ahlrichs, Balanced basis sets of split valence, triple zeta valence and quadruple zeta valence quality for H to Rn: Design and assessment of accuracy, Phys. Chem. Chem. Phys. **7**, 3297 (2005).

[175] D. Figgen, G. Rauhut, M. Dolg, and H. Stoll, Energy-consistent pseudopotentials for group 11 and 12 atoms: adjustment to multi-configuration Dirac–Hartree–Fock data, Chem. Phys. **311**, 227 (2005).

[176] K. A. Peterson, B. C. Shepler, D. Figgen, and H. Stoll, On the spectroscopic and thermochemical properties of ClO, BrO, IO, and their anions, J. Phys. Chem. A **110**, 13877 (2006).

[177] M. F. Peintinger, D. V. Oliveira, and T. Bredow, Consistent Gaussian basis sets of triple-zeta valence with polarization quality for solid-state calculations, J. Comput. Chem. **34**, 451 (2013).

[178] K. G. Dyall, Relativistic quadruple-zeta and revised triple-zeta and double-zeta basis sets for the 4p, 5p, and 6p elements, Theor. Chem. Acc. **115**, 441 (2006).

[179] K. G. Dyall, Relativistic double-zeta, triple-zeta, and quadruple-zeta basis sets for the 4d elements Y–Cd, Theor. Chem. Acc. **117**, 483 (2007).

[180] J. K. Desmarais, G. Ambrogio, G. Vignale, A. Erba, and S. Pittalis, Generalized Kohn-Sham approach for the electronic band structure of spin-orbit coupled materials, Phys. Rev. Mater. **8**, 013802 (2024).

[181] C. R. Berry, Physical defects in silver halides, Phys. Rev. **97**, 676 (1955).

[182] W. Hidshaw, J. T. Lewis, and C. V. Briscoe, Elastic constants of silver chloride from 4.2 to 300°K, Phys. Rev. **163**, 876 (1967).

[183] D. Vogel, P. Krüger, and J. Pollmann, *Ab initio* electronic structure of silver halides calculated with self-interaction and relaxation-corrected pseudopotentials, Phys. Rev. B **58**, 3865 (1998).

[184] A. H. Sommer, *Photoemissive Materials: Preparation, Properties and Uses*, 1st ed. (Wiley, New York, USA, 1986), Chap. 3, p. 21.

[185] P. Wang, B. Huang, X. Zhang, X. Qin, H. Jin, Y. Dai, Z. Wang, J. Wei, J. Zhan, S. Wang, J. Wang, and M.-H. Whangbo, Highly efficient visible-light plasmonic photocatalyst Ag@AgBr, Chem. Eur. J. **15**, 1821 (2009).

[186] F. Bassani, R. S. Knox, and W. B. Fowler, Band structure and electronic properties of AgCl and AgBr, Phys. Rev. **137**, A1217 (1965).

[187] G. Piermarini and C. Weir, A diamond cell for X-ray diffraction studies at high pressures, J. Res. Natl. Bur. Stand., Sect. A **66**, 325 (1962).

[188] S. Ves, D. Glötzel, M. Cardona, and H. Overhof, Pressure dependence of the optical properties and the band structure of the copper and silver halides, Phys. Rev. B **24**, 3073 (1981).

[189] J. P. Perdew and K. Schmidt, Jacob's ladder of density functional approximations for the exchange-correlation energy, AIP Conf. Proc. **577**, 1 (2001).

[190] J. C. Slater, A simplification of the Hartree–Fock method, Phys. Rev. **81**, 385 (1951).

[191] S. H. Vosko, L. Wilk, and M. Nusair, Accurate spin-dependent electron liquid correlation energies for local spin density calculations: a critical analysis, Can. J. Phys. **58**, 1200 (1980).

[192] J. P. Perdew, A. Ruzsinszky, G. I. Csonka, O. A. Vydrov, G. E. Scuseria, L. A. Constantin, X. Zhou, and K. Burke, Restoring the density-gradient expansion for exchange in solids and surfaces, Phys. Rev. Lett. **100**, 136406 (2008).

[193] J. P. Perdew, A. Ruzsinszky, G. I. Csonka, L. A. Constantin, and J. Sun, Workhorse semilocal density functional for

condensed matter physics and quantum chemistry, Phys. Rev. Lett. **103**, 026403 (2009).

[194] J. P. Perdew, A. Ruzsinszky, G. I. Csonka, L. A. Constantin, and J. Sun, Erratum: Workhorse semilocal density functional for condensed matter physics and quantum chemistry [Phys. Rev. Lett. **103**, 026403 (2009)], Phys. Rev. Lett. **106**, 179902(E) (2011).

[195] J. Tao and Y. Mo, Accurate semilocal density functional for condensed-matter physics and quantum chemistry, Phys. Rev. Lett. **117**, 073001 (2016).

[196] J. P. Perdew, S. Kurth, A. Zupan, and P. Blaha, Accurate density functional with correct formal properties: A step beyond the generalized gradient approximation, Phys. Rev. Lett. **82**, 2544 (1999).

[197] J. W. Furness, A. D. Kaplan, J. Ning, J. P. Perdew, and J. Sun, Accurate and numerically efficient r^2SCAN meta-generalized gradient approximation, J. Phys. Chem. Lett. **11**, 8208 (2020).

[198] J. W. Furness, A. D. Kaplan, J. Ning, J. P. Perdew, and J. Sun, Correction to "Accurate and numerically efficient r^2SCAN meta-generalized gradient approximation", J. Phys. Chem. Lett. **11**, 9248 (2020).

[199] See Supplemental Material at http://link.aps.org/supplemental/10.1103/PhysRevB.109.165144 for the following: basis-set study of silver halide crystals with nonrelaxed structure; density functional approximation study of silver halide crystals with relaxed structures, scalar-relativistic and spin-orbit results; further results for the indium(I,III)-telluride two-dimensional honeycomb system (results with the geometry optimization without D3-BJ correction for PBE, results with HSE06); energies and expectation values for the Pt chain with the canonical and the Scalmani-Frisch noncollinear ansatz for PBE as well as results with S-VWN (V) and TPSS; and all structures (coordinate files) used in this work.

[200] Minor deviations from the fcc structure were removed by symmetrization. This changed the energy by less than 3×10^{-4} hartree or less than 1 kJ/mol. Typically, changes are below 10^{-5} hartree.

[201] A. Patra, S. Jana, L. A. Constantin, and P. Samal, Efficient yet accurate dispersion-corrected semilocal exchange–correlation functionals for non-covalent interactions, J. Chem. Phys. **153**, 084117 (2020).

[202] S. Ehlert, U. Huniar, J. Ning, J. W. Furness, J. Sun, A. D. Kaplan, J. P. Perdew, and J. G. Brandenburg, r^2SCAN-D4: Dispersion corrected meta-generalized gradient approximation for general chemical applications, J. Chem. Phys. **154**, 061101 (2021).

[203] J. Heyd, G. E. Scuseria, and M. Ernzerhof, Hybrid functionals based on a screened Coulomb potential, J. Chem. Phys. **118**, 8207 (2003).

[204] J. Heyd, G. E. Scuseria, and M. Ernzerhof, Erratum: "Hybrid functionals based on a screened Coulomb potential" [J. Chem. Phys. **118**, 8207 (2003)], J. Phys. Chem. **124**, 219906 (2006).

[205] A. V. Krukau, O. A. Vydrov, A. F. Izmaylov, and G. E. Scuseria, Influence of the exchange screening parameter on the performance of screened hybrid functionals, J. Phys. Chem. **125**, 224106 (2006).

[206] L. Schimka, J. Harl, and G. Kresse, Improved hybrid functional for solids: The HSEsol functional, J. Chem. Phys. **134**, 024116 (2011).

[207] J. E. Moussa, P. A. Schultz, and J. R. Chelikowsky, Analysis of the Heyd-Scuseria-Ernzerhof density functional parameter space, J. Chem. Phys. **136**, 204117 (2012).

[208] J. Shang, L. Pan, X. Wang, J. Li, H.-X. Deng, and Z. Wei, Tunable electronic and optical properties of InSe/InTe van der Waals heterostructures toward optoelectronic applications, J. Mater. Chem. C **6**, 7201 (2018).

[209] R. H. M. Smit, C. Untiedt, A. I. Yanson, and J. M. van Ruitenbeek, Common origin for surface reconstruction and the formation of chains of metal atoms, Phys. Rev. Lett. **87**, 266102 (2001).

[210] V. M. García-Suárez, A. R. Rocha, S. W. Bailey, C. J. Lambert, S. Sanvito, and J. Ferrer, Conductance oscillations in zigzag platinum chains, Phys. Rev. Lett. **95**, 256804 (2005).

[211] A. Delin and E. Tosatti, Magnetic phenomena in $5d$ transition metal nanowires, Phys. Rev. B **68**, 144434 (2003).

[212] A. Delin and E. Tosatti, Emerging magnetism in platinum nanowires, Surf. Sci. **566-568**, 262 (2004).

[213] J. Fernández-Rossier, D. Jacob, C. Untiedt, and J. J. Palacios, Transport in magnetically ordered Pt nanocontacts, Phys. Rev. B **72**, 224418 (2005).

[214] A. Smogunov, A. Dal Corso, A. Delin, R. Weht, and E. Tosatti, Colossal magnetic anisotropy of monatomic free and deposited platinum nanowires, Nat. Nanotechnol. **3**, 22 (2008).

[215] J. Jaramillo, G. E. Scuseria, and M. Ernzerhof, Local hybrid functionals, J. Chem. Phys. **118**, 1068 (2003).

[216] P. Plessow and F. Weigend, Seminumerical calculation of the Hartree–Fock exchange matrix: Application to two-component procedures and efficient evaluation of local hybrid density functionals, J. Comput. Chem. **33**, 810 (2012).

[217] T. M. Maier, A. V. Arbuznikov, and M. Kaupp, Local hybrid functionals: Theory, implementation, and performance of an emerging new tool in quantum chemistry and beyond, Wiley Interdiscip. Rev.: Comput. Mol. Sci. **9**, e1378 (2019).

[218] C. Holzer and Y. J. Franzke, A local hybrid exchange functional approximation from first principles, J. Chem. Phys. **157**, 034108 (2022).